Electrical lead time during an extreme haboob-like dust-front intrusion in Ica, Peru

Rubén M. Romero[1,2], Rene Loayza[2], Gustavo Huaman[2], Dante Calderon[2], Yovanny Buleje[2], Joseph Arroyo[2], Miguel Tasayco[2], Cesar Torres[2], Jose Tacza[3], Sergio Szpigel[1], Jean-Pierre Raulin[1]

[1] Center for Radio Astronomy and Astrophysics Mackenzie, Engineering School, Mackenzie Presbyterian University, São Paulo, Brazil.
[2] Universidad Nacional San Luis Gonzaga, Ica, Peru.
[3] Institute of Geophysics, Polish Academy of Sciences, Warsaw, Poland.

Abstract:

Extreme dust storms evolving on sub-hourly timescales challenge conventional air-quality monitoring systems, as particulate matter (PM) sensors require sufficient aerosol accumulation before threshold exceedance is detected. The operational capability of atmospheric potential gradient (PG) measurements to provide early warning during rapidly evolving frontal dust intrusions remains insufficiently quantified.

We evaluate PG detection latency during an unusually intense haboob-like dust outbreak that impacted Ica, Peru (14.07°S, 75.73°W), on 31 July 2025. Two ground-based stations separated by 13.6 km recorded PG and $PM_{2.5}$ at minute-scale resolution. Frontal arrival times were independently constrained using GOES-19 ABI RGB imagery (10-min cadence) and 1-min ground-based cameras. Electrical detection was defined using objective seasonal baseline-departure criteria with multi-threshold persistence constraints.

PG exhibited an initial statistically significant deviation (2σ) at 12:25 LT, more than 100 minutes prior to local particulate enhancement. A conservative rapid-growth onset (5σ) occurred at 13:48 LT, preceding both the $PM_{2.5}$ increase at the urban station by 24 minutes and the camera-defined frontal impact by approximately 23 minutes. The event displayed a pronounced bipolar electrical structure, with PG amplification immediately before particulate onset followed by a sub-minute polarity reversal during frontal passage.

These results indicate that high-resolution PG monitoring captures organized boundary-layer electrification associated with density-current dust fronts and can extend actionable detection capability relative to mass-based aerosol sensors under extreme convective conditions.

Keywords:

Atmospheric electricity; potential gradient; dust storms; haboob; early warning

Graphical Abstract:

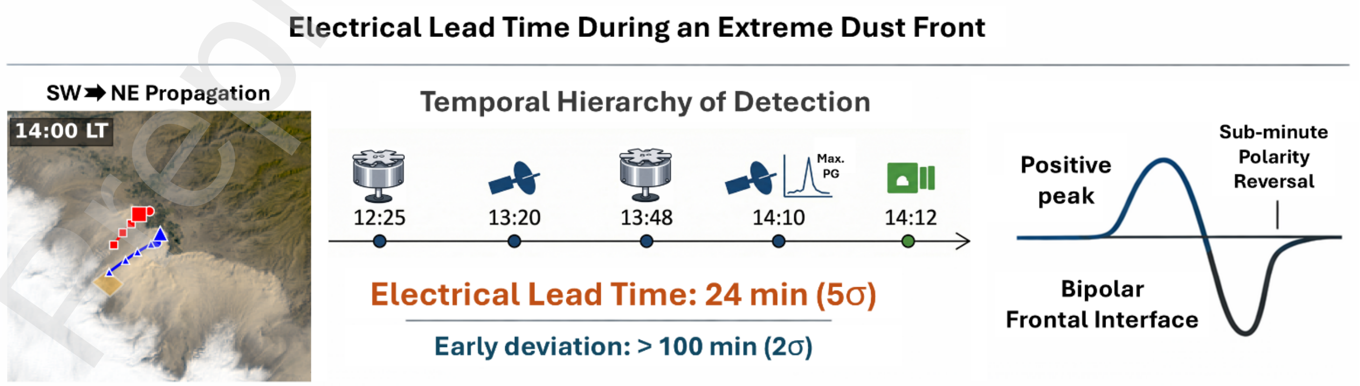

Highlights:

- 24-min electrical lead time relative to $PM_{2.5}$ during haboob-like dust front.
- Independent multi-platform timing constraints (satellite, cameras, sensors).
- Sub-minute bipolar polarity reversal during frontal passage.
- Electrical restructuring preceded measurable PM by >100 minutes (2σ stage).

1. Introduction:

Extreme dust storms pose major challenges for atmospheric monitoring and early-warning systems, particularly in arid and semi-arid regions where dust uplift can develop rapidly and with strong spatial heterogeneity. Short-lived, high-intensity dust events are often insufficiently represented within monitoring frameworks primarily designed around hourly or daily particulate matter (PM) reporting standards. Recent analyses demonstrate that daily averages may underestimate peak PM_{10} concentrations by more than an order of magnitude during sub-hourly convective dust outbreaks, thereby masking the true magnitude of acute exposure **(Ardon-Dryer & Aziz, 2025; Bouet et al., 2019)**. This limitation becomes especially critical during haboob-like frontal intrusions, where abrupt transitions in aerosol loading and visibility occur on timescales shorter than the temporal aggregation inherent to regulatory PM reporting practices **(Raman et al., 2014).**

Dust lifting and transport processes are intrinsically electrified. Field observations spanning several decades have documented large and rapid perturbations of the surface atmospheric electric field during dust storms, with amplitudes comparable to or exceeding those associated with thunderstorm-related disturbances **(Stow, 1969; Kamra, 1972; Harris, 1967).** More recent measurements have demonstrated minute-scale fluctuations reaching several kV m^{-1} during electrified dust events, closely associated with wind intensification and particulate loading **(Yair et al., 2016).** Observations of dust devils further show that vortex-induced charge separation can produce abrupt electric-field excursions exceeding typical fair-weather variability **(Franzese et al., 2018).** These findings indicate that dust-induced space-charge transport and conductivity modifications generate sharp electrical perturbations during rapidly evolving events.

Under fair-weather conditions, the atmosphere sustains a persistent vertically directed electric field maintained by the Global Atmospheric Electric Circuit, driven by worldwide thunderstorm activity **(Wilson, 1921; Rycroft et al., 2000).** At the surface, this field is commonly expressed as the atmospheric potential gradient (PG), defined as PG = $-E_z$, where Ez is the vertical electric field taken as positive upward **(Chalmers, 1954)**. Over oceans, fair-weather PG values are relatively stable, typically on the order of 10^2 V m^{-1}, as established by the Carnegie expedition measurements **(Harrison, 2013)**. Over continental surfaces, however, PG is strongly modulated by boundary-layer processes including aerosol loading, turbulent mixing, and local space-charge formation. During dust intrusions, both conductivity reduction and advected space-charge layers may substantially perturb PG at the surface.

Despite extensive documentation of dust-induced electrical variability, the temporal relationship between electrical disturbance and particulate-mass enhancement during extreme frontal dust events remains insufficiently quantified. In particular, whether high-resolution PG monitoring can provide operationally meaningful lead time relative to conventional PM sensors during haboob-like density-current intrusions has not been systematically evaluated.

In the southern Peruvian coastal desert, Paracas dust storms constitute the dominant regional dust phenomenon. These events are predominantly non-convective and are driven by strong alongshore pressure gradients and synoptic-scale forcing associated with anticyclonic circulation over the southeastern Pacific and northern Chile. Satellite analyses, reanalysis data, and trajectory modeling have established the characteristic source regions, transport pathways, and meteorological drivers of Paracas events **(Briceño-Zuluaga et al., 2017).** Complementary long-term ground-based measurements at Ica demonstrate that typical Paracas storms are consistently recorded as marked negative PG disturbances under well-defined wind regimes, associated with aerosol transport and dust electrification processes **(Romero et al., 2024).** Together, these studies establish the characteristic synoptic forcing and recurrent PG response associated with typical Paracas dust intrusions.

Despite this well-documented regime, published descriptions generally characterize Paracas events as wind-driven dust intrusions with gradual inland transport rather than as sharply defined, vertically organized frontal structures comparable to classical haboobs reported in other arid regions **(Briceño-Zuluaga et al., 2017).** The established Paracas framework emphasizes synoptic forcing and pressure-gradient enhancement over sharply defined dust walls exhibiting density-current–type morphology. Whether the surface PG response under such structurally distinct dust-front intrusions departs from the established Paracas electrical regime has not yet been explicitly examined.

On 31 July 2025, an unusually intense dust outbreak impacted the city of Ica, Peru. Satellite imagery documented rapid inland expansion of a sharply defined advancing dust wall, and local observations reported abrupt visibility reduction and strong winds. Independent regional reports also confirmed the widespread extent of the outbreak **(NASA Earth Observatory, 2025; El Comercio, 2025)**. The event exhibited characteristics more consistent with a density-current–like frontal intrusion than with the gradual dust enhancement typical of canonical Paracas storms. This outbreak therefore provides a natural stress-test case to evaluate the performance of PG monitoring under extreme and dynamically organized dust conditions.

In this study, we assess the operational viability of PG measurements as an early-response indicator during this extreme dust intrusion. Two ground-based stations separated by 13.6 km recorded PG and $PM_{2.5}$ at minute-scale resolution. Satellite RGB imagery from the Geostationary Operational Environmental Satellites (GOES-19) Advanced Baseline Imager (ABI), providing full-disk coverage at 10-minute cadence **(Schmit et al., 2005)**, was used to define objective frontal arrival times over the monitoring corridor. Ground-based cameras operating at 1-minute cadence provided additional independent temporal constraints. Using objective seasonal baseline-departure criteria, we quantify the latency between electrical perturbation, satellite-defined frontal arrival, visual impact, and PM response.

The analysis focuses exclusively on detection timing and lead time rather than on dust concentration or event attribution. By restricting the investigation to a single extreme outbreak, the study adopts an operational stress-test framework to determine whether PG monitoring provides measurable electrical lead time under rapidly evolving dust-front conditions and whether electrical restructuring precedes surface mass loading in a manner that complements conventional PM-based monitoring systems.

2. Data

2.1 Study Area and Monitoring Network

The study was conducted in the Ica region, southern Peru (14.07°S, 75.73°W), located within the hyper-arid coastal desert belt of the south-central Peruvian coast **(Gay, 2005; Briceño-Zuluaga et al., 2017).** The area is seasonally affected by strong austral winter winds that promote dust emission from coastal source regions and inland transport toward the urban basin of Ica.

The monitoring network consists of two ground-based stations separated by approximately 13.6 km along a north–south axis. The main station, hereafter referred to as **CST** (CIEASEST), is located at the Centro de Investigación de la Actividad Solar y sus Efectos sobre la Tierra (Solar Activity and Terrestrial Effects Research Center). The secondary station, hereafter referred to as **STG** (Santiago), is situated in the district of Santiago, south of CST. This spatial configuration enables evaluation of dust-front progression across the urban corridor during extreme events. **Figure 1** presents the study area and the relative positions of CST and STG within the Ica region.

Figure 1. Geographical setting of the study area in the Ica region, Peru. The satellite imagery shows the location of the **CIEASEST (CST)** and **Santiago (STG)** monitoring stations. The inset map (top right) indicates the regional context within Peru. The dashed line marks the geodesic distance (**13.6 km**) between the sites, established as the baseline to evaluate the spatiotemporal progression of the extreme dust event on July 31, 2025.

2.2 PG Measurements

PG was measured at CST using a BOLTEK EFM-100 field mill installed at approximately 0.5 m above ground level. The CST station forms part of the South American Atmospheric Electric Field Network (AFINSA), whose instrumentation framework and calibration procedures are described in Tacza et al. (2014). The instrument operates through a rotating shutter mechanism that periodically exposes and shields sensing electrodes from the ambient vertical electric field. When exposed, electric charge is induced on the electrodes and flows through a sensing resistor; when shielded, the charge returns to ground. This periodic charge displacement generates an AC signal proportional to the ambient PG. The internal electronics rectify and digitize the signal, providing measurements within a range of ±20 kV m^{-1}, with 0.01 kV m^{-1} digital resolution and a nominal response time of 0.1 s.

Because the permanent EFM sensor is installed above ground level, all measurements are corrected to their ground-reference equivalent using station-specific calibration coefficients derived from simultaneous reference–permanent sensor regression analysis, following the methodology described in Tacza (2015). Consequently, although the raw instrumental output spans ±20 kV m^{-1}, the effective full-scale range in corrected units for the Ica station is approximately ±4.1 kV m^{-1}. All PG values reported in this study correspond to these corrected ground-equivalent electric field values.

The native acquisition frequency was configured at 2 Hz (sampling interval of 0.5 s). For detection-latency analysis, PG data were aggregated to 1-minute resolution to harmonize the time base with the other datasets used for timing comparisons. This temporal aggregation also reduces sub-minute variability without affecting the event-scale onset timing metrics reported here. High-resolution (5 s) PG data were retained and analyzed separately to resolve the fine-scale polarity reversal during frontal passage (Section

4.3). Long-term performance, site-specific fair-weather criteria, and dominant atmospheric controls at CST have been comprehensively documented previously **(Romero et al., 2024).** In the present study, only data from 31 July 2025 were analyzed.

2.3 Particulate Matter Measurements

Particulate matter concentrations were measured at both CST and STG using PurpleAir Flex optical sensors based on laser light scattering. The instruments provide mass-equivalent concentrations for $PM_{1.0}$, $PM_{2.5}$, and PM_{10}. In this study, the atmospheric mass-equivalent $PM_{2.5}$ concentration (expressed in $\mu g\ m^{-3}$) was analyzed, as it represents fine dust transported during Paracas events and provides the most direct comparison with PG variability. Each sensor contains two independent measurement channels (A and B), allowing internal consistency assessment. The native temporal resolution is 2 minutes. Raw 2-minute $PM_{2.5}$ data were used without additional temporal smoothing, as the present analysis focuses on onset timing rather than absolute concentration magnitude.

2.4 Surface Meteorological Observations

Surface meteorological measurements were available at both monitoring sites. At CST, two co-located cup anemometers and wind vanes were mounted on the same tower at 2 m (A1) and 10 m (A2) above ground level, providing wind speed and wind direction measurements at 10 s temporal resolution. Solar irradiance at CST was likewise recorded at 10 s resolution. At STG, wind speed was recorded at 1 min temporal resolution. For consistency with the primary PG and $PM_{2.5}$ analyses, CST meteorological data were averaged to 1 min resolution unless otherwise specified. High-resolution (10 s) CST data were used exclusively for the fine-scale timing assessment of frontal passage presented in Section 4.3 and Appendix B. In this study, wind speed, wind direction, and solar irradiance were used to characterize the abrupt dynamical transition associated with frontal passage. The two-level wind configuration at CST enables assessment of vertical flow structure during the pre-surge and post-impact phases of the dust front.

2.5 Satellite Observations and Dust-Front Arrival Time

Geostationary satellite observations were obtained from the NOAA GOES-19 Advanced Baseline Imager (ABI), operating in the GOES-East position at 75.2°W during the study period. Level 2 Cloud and Moisture Imagery Full-Disk (CMIPF) products were accessed through the NOAA Open Data Dissemination (NODD) program via the publicly available AWS S3 bucket (noaa-goes19, us-east-1 region). Calibrated CMI fields from ABI channels C01, C02, and C03 were used to generate True Color RGB composites. GOES-19 ABI provides imagery at nominal 10-minute cadence for the full-disk scan used in this study. True Color RGB composites were constructed from the CMI fields using the native geostationary projection metadata. Satellite acquisition times correspond to the observation timestamps embedded in the product metadata.

During real-time monitoring of this specific event, the most recent publicly accessible GOES imagery available through the NODD AWS distribution lagged the nominal acquisition timestamp by approximately 20 minutes, as determined by comparison between product metadata timestamps and the local system time at the monitoring site. This delay reflects operational data availability through the public dissemination pathway rather than intrinsic satellite acquisition timing.

2.6 Visual Documentation

Ground-based visual documentation of the event was obtained using fixed cameras installed at CST and STG. The imagery was used qualitatively to confirm the timing and structure of dust-front arrival. Camera model specifications are not included, as the images were not used for quantitative analysis.

3. Methods

3.1 Event overview

On 31 July 2025, an intense dust storm impacted the city of Ica, Peru, producing a sharply defined advancing dust front and rapid inland expansion across the monitoring corridor. The event was accompanied by abrupt visibility reduction and strong surface winds at the time of frontal passage. Satellite imagery documented widespread dust coverage over coastal Peru on the same day (NASA Earth Observatory, 2025), while contemporaneous regional media reports described sudden dust engulfment affecting Ica, Paracas, Pisco, and Nasca (El Comercio, 2025).

Based on its well-defined leading boundary and rapid frontal progression, the event is described here as haboob-like, referring to a density-current–type dust-front intrusion exhibiting organized frontal geometry and sudden near-surface forcing. This designation is used in a structural sense and does not imply direct thermodynamic characterization. The event is treated as a single-case timing experiment designed to quantify the relative response of the PG, satellite detection, and particulate monitoring systems during a rapidly evolving dust-front intrusion. All times reported are expressed in local time (LT, UTC−5).

3.2 Satellite-based dust-front timing

The satellite reference time was defined by manual visual inspection of GOES True Color RGB imagery as the first full-disk frame in which dust-associated pixels corresponding to the leading edge of the plume became clearly identifiable within a predefined region of interest encompassing the Ica monitoring corridor. No automated detection algorithm, spectral thresholding, or quantitative dust index was applied. Timing was determined directly from visually distinguishable dust signatures in the RGB composite imagery.

Given the 10-minute temporal resolution of the full-disk imagery, the satellite timing uncertainty is bounded by ±5 minutes. The satellite timing serves as an independent regional reference against which ground-based detection latency is evaluated. The regional frontal propagation velocity was estimated from the displacement of the visually identified leading edge between consecutive frames divided by the corresponding time interval.

3.3 Definition of $PM_{2.5}$ detection time

$PM_{2.5}$ onset at each station was detected on the native 2-min sampling grid using a baseline-relative change-point criterion. For the same local time window (13:30–14:20 LT), a robust background baseline was constructed from the previous five days using the median and MAD. Onset was defined as the first time when (i) the 2-min rate-of-rise and (ii) the $PM_{2.5}$ level simultaneously exceeded their respective baseline envelopes (rate: median + 3×MAD; level: median + 1×MAD) for two consecutive bins (4 min persistence). This definition isolates abrupt frontal intrusions while remaining independent of fixed absolute thresholds. Although PM1.0, PM2.5, and PM10 were recorded at both stations, all size fractions exhibited coincident onset times within the 2-min resolution for this event; therefore, only PM2.5 is presented for clarity.

3.4 Definition of PG detection time

The electrical detection time $t_{PG}$was defined using a seasonal climatological baseline rather than a local pre-event interval. Hourly July mean (μ_h) and standard deviation (σ_h) values derived from the long-term PG climatology established in **Romero et al. (2024)**, were interpolated to minute resolution to construct a time-dependent baseline $\mu(t)$and $\sigma(t)$. This approach ensures that detection thresholds reflect typical diurnal variability rather than short pre-event fluctuations.

Electrical onset was defined as the first sustained exceedance of a kσ threshold:

$$PG(t) > \mu(t) + k\sigma(t)$$

Detection was restricted to times after 12:00 LT to exclude the morning transition period, during which PG variability may be influenced by fog-related and boundary-layer effects documented for this region **(Romero et al., 2024)**, rather than by frontal dust dynamics. To ensure robustness against transient noise, exceedance was required to persist for at least five consecutive minutes.

Multiple thresholds were evaluated to characterize hierarchical electrical evolution. A 2σ criterion defines the earliest statistically significant departure from seasonal variability. A 4σ criterion marks intermediate strengthening beyond moderate variability. A conservative 5σ criterion isolates the onset of the rapid-growth regime associated with dynamically forced electrification. In the present framework, the 5σ crossing defines the transition time into potential accelerated growth, while the persistence and magnitude of subsequent PG amplification characterize the physical severity of the event. This multi-threshold approach therefore distinguishes early statistical departure (2σ), intermediate strengthening (4σ), and transition into dynamically forced electrical growth (5σ), rather than functioning as a purely binary alarm system.

For contextual comparison of event magnitude, daily PG extrema were computed from the complete 2018–2025 minute-resolution dataset. For each calendar day, the daily maximum and minimum PG, the maximum absolute PG (MaxAbs), and the peak-to-trough excursion (ΔPG) were derived. Days with fewer than 1000 valid minute samples (~70% daily coverage) were excluded to avoid bias from incomplete daily records.

3.5 Detection latency and propagation metrics

Detection latency relative to the satellite reference was evaluated by comparing ground-based detection times (PG and $PM_{2.5}$) with the satellite-defined frontal intersection time, acknowledging the ±5 min uncertainty imposed by the 10-min imagery cadence. Electrical lead time at CST was defined as the time difference between PG detection and local $PM_{2.5}$ onset. Frontal propagation between stations was defined as the time difference between $PM_{2.5}$ onset at STG and CST. These metrics quantify both corridor-scale advection and relative sensor response timing.

4. Results

4.1 Regional formation and propagation of the 31 July 2025 dust front

Geostationary satellite imagery (GOES-19) indicates that the 31 July 2025 dust storm originated southwest of the Ica urban corridor and propagated northeastward as a coherent and sharply defined frontal structure at regional scale. The spatiotemporal evolution of the event is shown in **Figure 2**, where the dust-storm initiation area is delineated by an orange polygon. The first unambiguous identification of the dust front within this source region occurred at 13:20 LT (18:20 UTC), defining the satellite-based regional reference time. At 13:20 LT, the leading edge of the dust plume was located at 14.32°S, 75.86°W, approximately 7.6 km southwest of the STG station. From this position, the frontal system advanced northeastward toward the monitoring corridor.

Satellite tracking reveals that the event evolved into two quasi-parallel frontal segments propagating along a consistent southwest-to-northeast axis. The first segment became clearly established along the STG-directed trajectory shortly after 13:20 LT and reached the vicinity of STG at approximately 14:00 LT. A second dust plume organized approximately 10 minutes later (≈13:30 LT) along a slightly offset trajectory aligned with the CST sector and subsequently reached the vicinity of CST at approximately 14:10 LT. Although both segments originated from the same regional outbreak and were driven by the same large-scale forcing, the CST impact was associated with this later-forming plume rather than with simple advection of an identical rigid frontal boundary.

The total regional transit time between the initial satellite identification southwest of STG (13:20 LT) and satellite-detected arrival in the CST sector (≈14:10 LT) is approximately 50 minutes. This interval represents the large-scale propagation time of the frontal system across the monitoring corridor. Because GOES imagery is available at 10-minute cadence, satellite arrival times correspond to the nearest available frame in which the front is identifiable within each sector and may therefore slightly lag higher-resolution ground-based visual identification.

An independent estimate of propagation speed can be derived from the particulate onset difference between STG and CST. Using the 13.6 km station separation and the 16-minute delay between PM$_{2.5}$ onsets yields an effective corridor-scale speed of approximately 14.2 m s^{-1} (51 km h^{-1}). Because the event consisted of two closely related frontal segments rather than a single rigid boundary, this value should be interpreted as an effective transit rate across the corridor rather than strict advection of an identical front. The similarity in magnitude between this corridor-scale rate and the satellite-derived regional velocity indicates dynamically organized southwest-to-northeast propagation across multiple spatial scales. **Figure 2** presents the complete satellite sequence (13:10–14:20 LT), documenting the regional formation and subsequent approach to the Ica monitoring corridor.

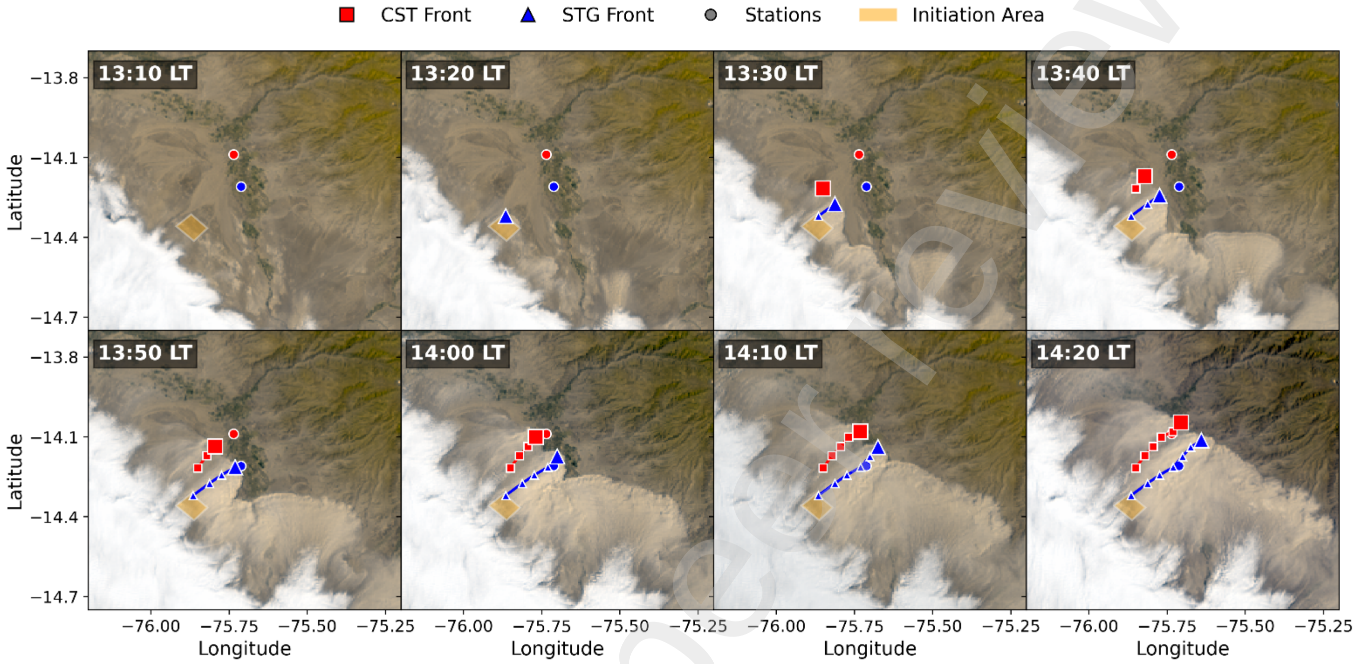

Figure 2. Spatiotemporal evolution of the dust front derived from GOES-19 RGB imagery sequence (13:10 – 14:20 LT). The orange polygon delineates the identified dust-storm initiation area southwest of the monitoring corridor. The advancing frontal boundary is tracked at 10-minute intervals, distinguished by propagation path: red squares indicate the wavefront trajectory toward the CST station, and blue triangles indicate the trajectory toward the STG station.

4.2 Visual local arrival of the dust front (camera observations)

The local arrival of the dust front was independently constrained using ground-based camera imagery at both monitoring sites. Images were acquired at 1 min temporal resolution, providing time-resolved visual documentation of frontal progression across the monitoring corridor. Representative frames from both stations are shown in Figure 3.

At STG, the westward-oriented camera captured the dust wall propagating from southwest to northeast across the station field of view, with a dominant meridional (south-to-north) component. Visual inspection of the image sequence shows that at 13:56 LT the leading edge of the haboob is clearly identifiable immediately adjacent to the station domain. In the subsequent frame at 13:57 LT, the dust wall has already advanced beyond the station location, constraining frontal crossing to the interval between these two frames. Given the 1 min acquisition interval, 13:56 LT is conservatively adopted as the visual arrival time at STG, with temporal precision limited by the image sampling resolution.

Concurrent surface meteorological observations at STG confirm the frontal character of the event. Wind speed increased from 3.0 m s^{-1} at 13:56 LT to 12.4 m s^{-1} at 13:57 LT, while solar irradiance decreased abruptly from 555 W m^{-2} to 33 W m^{-2} within the same minute. This sharp dynamical and radiative transition is consistent with passage of a density-current–like dust front rather than gradual aerosol advection.

At CST, the same westward-oriented configuration recorded the dust front advancing from southwest to northeast toward the station, with a dominant zonal component that produced a near-frontal visual interception. The first distant visual signature of the dust wall is discernible in the 13:52 LT frame near the Huacachina dune field. By 14:04 LT, the wall appears fully developed, exhibiting a clearly defined vertical structure advancing toward the urban boundary. At 14:11 LT, the dust front visibly intersects the CST station domain, defining the local impact time. All timestamps are derived from the same time-resolved camera sequence. The complete image sequence used to constrain the visual timing analysis is archived in a permanent public repository **(Romero et al., 2026).** The visually determined 14:11 LT arrival at CST is used as the physical impact reference and compared with instrument-derived detection times in Section 4.3.

High-resolution (10 s) surface observations at CST provide additional temporal constraints on frontal impact. Solar irradiance remained stable near 720–750 W m^{-2} until 14:11:50 LT, after which a sharp decline occurred: irradiance decreased to 539 W m^{-2} at 14:12:00 LT and further to 284 W m^{-2} at 14:12:10 LT, representing an approximate 50% reduction within 20 s. A local minimum of 219 W m^{-2} was reached at 14:13:00 LT. Concurrently, wind speed increased from near-calm conditions to 3.3 m s^{-1} at 14:12:00 LT, exceeded 7 m s^{-1} by 14:12:20 LT, and reached 9.0 m s^{-1} at 14:13:20 LT. The onset of the radiative collapse and wind intensification at 14:12:00 LT confirms the arrival of the optically densest frontal core at CST.

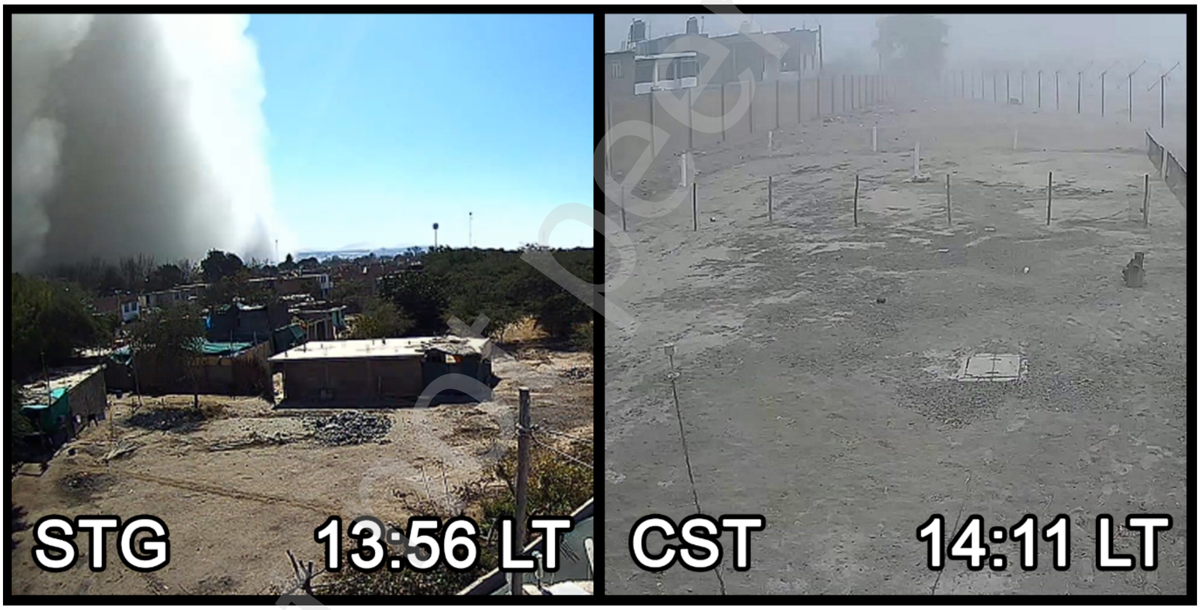

Figure 3. Ground-based camera images documenting the local arrival of the 31 July 2025 dust front at STG (13:56 LT, left) and CST (14:11 LT, right). Both cameras were oriented westward.

4.3 Electrical and particulate detection times at ground stations

Figure 4 illustrates the temporal evolution of PG at CST together with PM$_{2.5}$ at STG and CST during the 31 July 2025 dust event. A clear spatiotemporal progression is observed across the two stations. The earliest statistically significant electrical departure (2σ threshold) occurs at 12:25 LT, marking the first robust deviation from seasonal variability. At this time, PG reaches 184 V m^{-1}, exceeding the expected background envelope. Progressively stricter criteria reveal a hierarchical strengthening sequence. A sustained 4σ exceedance is reached at 13:21 LT, indicating intensified electrical departure. A further escalation to the 5σ level occurs at 13:48 LT, coinciding with the onset of a pronounced acceleration phase in the PG. This 5σ transition marks the shift from gradual deviation to dynamically forced growth preceding frontal arrival.

At the southern station (STG), $PM_{2.5}$ onset is detected at 13:56 LT, corresponding to frontal arrival at that location. $PM_{2.5}$ at CST exhibits a sharp increase at 14:12 LT, marking impact at the main station. The temporal difference between STG and CST particulate onsets is 16 minutes, consistent with northward advection across the ~13.6 km station separation. The 2σ electrical detection at 12:25 LT precedes $PM_{2.5}$ onset at STG and CST by approximately 91 and 107 minutes, respectively. Even under the more conservative 5σ criterion, the electrical rapid-growth onset at 13:48 LT precedes CST particulate arrival by approximately 24 minutes. Thus, substantial electrical lead time persists across detection sensitivities.

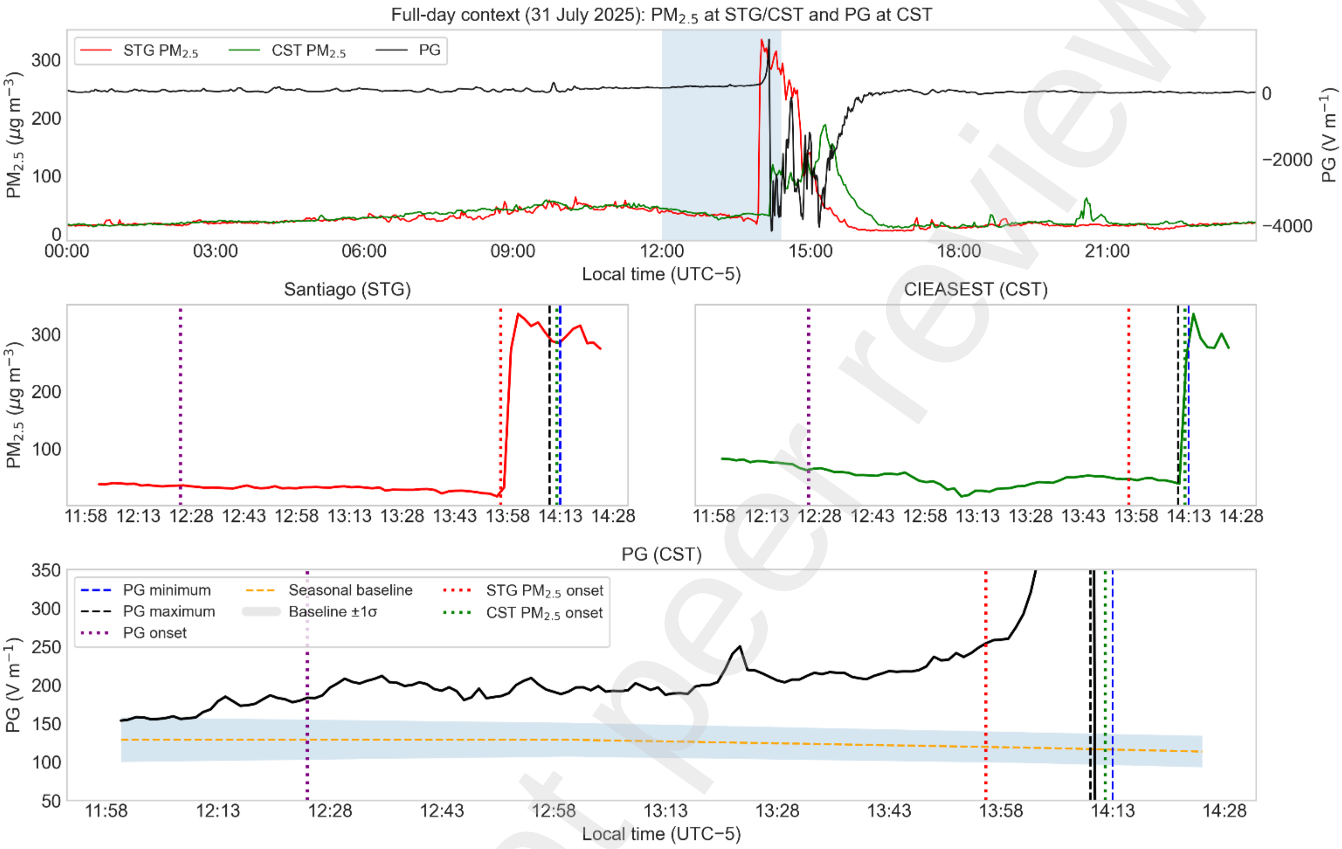

Figure 4. Temporal evolution of PG at CST and $PM_{2.5}$ at STG and CST on 31 July 2025. The upper panel shows the full-day context, with the shaded region marking the event window. Middle panels display $PM_{2.5}$ at STG and CST, and the lower panel shows PG at CST. Vertical lines indicate the earliest electrical detection (2σ) and particulate onset times at both stations, together with key PG extrema. PG detection at 12:25 LT precedes $PM_{2.5}$ onset at STG (13:56 LT) and CST (14:12 LT).

To evaluate short-term false-trigger behavior under seasonally consistent conditions, the same kσ + 5-min persistence detector was applied to the 30 days preceding 31 July 2025 within the identical 12:00–14:15 LT window (July-only background). Under the conservative 5σ criterion, one non-event day (1/30) exhibited a threshold crossing. However, in that case the PG increased by only ~13 V m^{-1} within the subsequent 60 minutes and reached its local maximum within 1 minute of threshold crossing, indicating the absence of sustained amplification. In contrast, on 31 July 2025 the PG increased by ~1390 V m^{-1} within 22 minutes following the 5σ crossing, marking the onset of a dynamically forced growth regime.

These results demonstrate that while isolated 5σ crossings may occur within background variability, extreme density-current events are uniquely characterized by sustained post-onset amplification. Thus, the 5σ threshold functions not as a binary event discriminator, but as a physically meaningful marker of transition into rapid electrical growth. The complete chronology of satellite, visual, electrical, and particulate detection times is summarized in **Table 1.**

To examine the fine-scale dynamics of frontal passage, **Figure 5** presents the temporal co-evolution of PG and $PM_{2.5}$ at CST. At 1-min resolution, PG increases from approximately 224 V m^{-1} at 13:48 LT to a local maximum of +1614 V m^{-1} at 14:10 LT. Immediately thereafter, the signal undergoes an abrupt polarity reversal, reaching −936 V m^{-1} at 14:11 LT, −3663 V m^{-1} at 14:12 LT, and a minimum of −4167 V m^{-1} at 14:13 LT. The resulting peak-to-minimum excursion approaches 5.8 kV m^{-1} within approximately three minutes, and the largest one-minute decrease (14:11–14:12 LT) exceeds −2.7 kV m^{-1}. This rapid transition indicates substantial reconfiguration of the electric field during passage of the densest portion of the dust front.

Table 1. Chronology of visual arrival and instrument-derived detection times for the 31 July 2025 dust event.

Parameter	Time (LT)	Definition
PG exceedance (2σ, CST)	**12:25**	2σ exceedance (persistent)
Satellite-defined initiation (L_0)	13:20	First detection of frontal boundary (FB)
PG exceedance (4σ, CST)	13:21	4σ exceedance (persistent)
PG exceedance (5σ, CST)	13:48	5σ exceedance (persistent)
Visual arrival (STG)	13:56	FB arrival at station
$PM_{2.5}$ onset (STG)	13:56	Baseline rate + persistence
Satellite arrival (STG)	14:00	FB enters STG sector
Satellite arrival (CST)	14:10	FB enters CST sector
PG maximum (CST)	14:10	Local maximum prior to PM step
Visual arrival (CST)	14:11	FB arrival at station
$PM_{2.5}$ onset (CST)	14:12	Baseline rate + persistence
PG minimum (CST)	14:13	Abrupt polarity reversal
PG–$PM_{2.5}$ lead time (2σ, CST)	107 min	2σ PG to $PM_{2.5}$ onset (CST)
PG–$PM_{2.5}$ lead time (5σ, CST)	24 min	5σ PG to $PM_{2.5}$ onset (CST)
Propagation time (STG→CST)	16 min	$PM_{2.5}$ onset STG to CST

While the 1-min series captures the overall excursion, higher-resolution measurements further resolve the internal structure of the reversal. Five-second PG data reveal a sharper pre-frontal maximum of +1847 V m^{-1} at 14:11:00 LT, followed by a polarity crossing within a single 5 s sampling interval, from +296 V m^{-1} at 14:11:20 LT to −917 V m^{-1} at 14:11:25 LT. This corresponds to a decrease of approximately 1213 V m^{-1} over 5 s (mean rate ≈ −243 V m^{-1} s^{-1}), demonstrating extremely rapid electric-field restructuring.

At the time of this electrical transition, the near-surface anemometer A1 (2 m) remained within a short pre-surge low-wind interval, recording 0.0 m s^{-1} between 14:10:40 and 14:11:50 LT, whereas the upper-level anemometer A2 (10 m) indicated sustained non-zero flow and gradual strengthening during the same period. Solar irradiance likewise remained high through 14:11:50 LT (~748 W m^{-2}), indicating that neither pronounced radiative attenuation nor the near-surface outflow surge had yet begun. Wind direction during this interval exhibited substantial variability at both levels, without a stable sectoral alignment.

The radiative collapse and near-surface wind intensification begin at 14:12:00 LT, when irradiance drops abruptly and the 2 m anemometer transitions from calm to sustained outflow. This dynamical transition occurs ~35 s after the electrical polarity reversal, indicating that the leading electrical boundary precedes arrival of the optically dense and dynamically forced core at the sensor location.

PG subsequently intensified negativeward, reaching −4167 V m^{-1} at 14:12:25 LT and remaining at this value until 14:14:45 LT, forming a sustained ~140 s plateau. This persistence at an identical minimum indicates that the signal reached the effective corrected full-scale limit of the measurement system (Section 2.2), implying that the true peak negative electric field during frontal core passage may have exceeded the reported value. In contrast to the three-minute excursion evident at 1-min resolution, the most intense phase of the reversal unfolded within approximately 85 s, demonstrating that the electrical transition was highly structured and rapidly evolving rather than a gradual drift. The complete high-resolution PG, irradiance, and two-level wind time series used to determine these timings are provided in Appendix B (Figure B1).

To evaluate the magnitude of the electrical excursion relative to long-term variability, the 31 July 2025 event was compared against the multi-year daily PG distribution derived from the 2018–2025 minute-resolution record (N = 2620 days; see Methods). The event reached MaxAbs = 4167 $V\ m^{-1}$ and ΔPG = 5780 $V\ m^{-1}$, exceeding the 99.9th percentile of the historical distribution (MaxAbs p99.9 = 3552 $V\ m^{-1}$; ΔPG p99.9 = 5452 $V\ m^{-1}$). No other day in the filtered 2018–2025 record surpasses these thresholds, indicating that this event represents the most extreme daily electrical excursion in the available multi-year dataset. A complementary regime comparison with canonical Paracas events is provided in Appendix C, where PG-centered epoch analysis confirms that the bipolar structure observed on 31 July 2025 is not characteristic of typical wind-driven Paracas episodes.

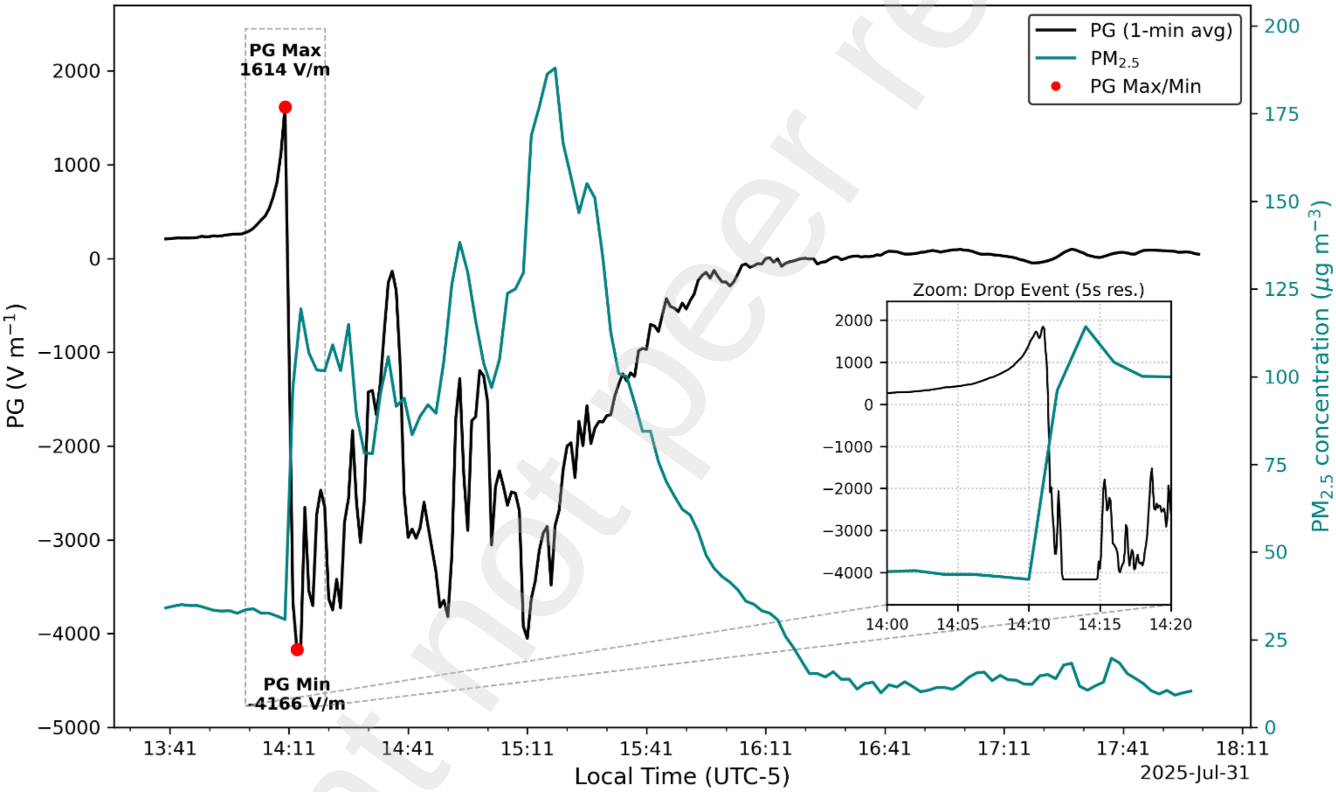

Figure 5. Temporal evolution of PG and normalized $PM_{2.5}$ concentration at the CST station on 31 July 2025. The main panel shows the 13:40–18:00 LT observation window, with red markers denoting the local PG maximum and subsequent minimum. The inset provides a magnified view of the 14:00–14:20 LT period capturing the fine-scale dynamics during the particulate front arrival.

Although multiple CST $PM_{2.5}$ sub-peaks are observed during the subsequent mature phase (14:50–15:20 LT), no additional polarity reversals or comparably abrupt PG excursions are detected. PG remains within a sustained negative regime and evolves smoothly during these later aerosol enhancements. This indicates that the strongest electrical structure is temporally confined to the leading boundary of the dust front rather than to later phases of maximum surface mass loading.

Comparison with independently determined visual arrival times further constrains detection latency. At STG, the camera-defined arrival at 13:56 LT is coincident with the $PM_{2.5}$ onset at 13:56 LT within the 2-min sampling resolution of the particulate measurements, indicating that the step-like PM increase occurs essentially at the time of frontal crossing at this site. At CST, the visually determined impact at 14:11 LT is nearly coincident with the $PM_{2.5}$ onset at 14:12 LT, corresponding to an offset of approximately one minute, well within the 2-min cadence of the sensor. In contrast, the 2σ electrical deviation at 12:25 LT precedes visual impact by approximately 106 min, while the 5σ rapid-growth onset at 13:48 LT precedes visual impact by approximately 23 min.

Together, these observations define a temporally ordered sequence consisting of early electrical departure, hierarchical strengthening, rapid pre-frontal maximum, and abrupt bipolar transition during frontal passage. This ordering confirms south-to-north propagation and demonstrates that electrical perturbation develops substantially in advance of measurable local aerosol concentration enhancement.

5. Discussion

The 31 July 2025 dust event provides a structured, multi-instrument demonstration that detection latency in conventional particulate monitoring during rapidly evolving convective dust intrusions is fundamentally governed by temporal dynamics rather than by sensor absence. The observed sequence, consisting of early electrical disturbance at CST, subsequent particulate onset at STG, and later onset at CST, reveals a coherent south-to-north progression consistent with satellite-derived regional propagation. The separation between the rapid-growth electrical onset and local $PM_{2.5}$ arrival at CST, together with the earlier statistically defined baseline departure at 12:25 LT, defines a measurable and operationally relevant temporal advantage of PG relative to mass-based aerosol detection at the same site.

5.1 Coherent regional propagation and temporal hierarchy

Satellite RGB imagery constrained the regional formation of the dust front south of the monitoring corridor at 13:20 LT and documented organized northward transport. However, the 10-minute acquisition cadence of GOES imagery imposes discretization limits on minute-scale arrival determination at fixed sensor locations. Furthermore, publicly distributed satellite products may exhibit dissemination latency relative to acquisition time.

During this event, ground-based visual confirmation of the approaching dust wall preceded the availability of the corresponding satellite frame for analysis. This reflects the practical difference between nominal acquisition timestamps and the effective time at which imagery becomes accessible through public distribution portals, which may introduce variable operational delays. This distinction between acquisition time and dissemination time is operationally important, as it constrains the immediacy of satellite-only nowcasting during rapidly evolving dust events.

The consistency between satellite-derived regional propagation speed (~12.7 m s^{-1}) and station-to-station $PM_{2.5}$ onset speed (~14.2 m s^{-1}) supports interpretation of a dynamically organized outbreak rather than diffuse aerosol enhancement. The difference between frontal translation speed and peak wind gusts (reported regionally up to ~90 km h^{-1}) reflects the distinction between system-scale advection and localized instantaneous wind maxima within the density current. Frontal propagation represents an integrated mesoscale process controlled by density contrasts, boundary-layer stratification, and surface friction, whereas gusts capture transient dynamic peaks. The electrical lead time therefore relates to frontal dynamics rather than to peak wind magnitude alone.

Camera-based arrival times further confirm spatial coherence. At both STG and CST, visual arrival either precedes or nearly coincides with the abrupt $PM_{2.5}$ step increase, demonstrating that the particulate response corresponds to physical frontal intersection rather than gradual accumulation. In contrast, the PG disturbance at CST develops well before visual impact, indicating sensitivity to boundary-layer restructuring ahead of the visible dust wall. The sensitivity of PG measurements to dynamical restructuring within the planetary boundary layer has been demonstrated in previous studies **(Nicoll et al., 2018)**, supporting interpretation of early PG deviations as signatures of evolving boundary-layer structure rather than direct surface mass loading.

Importantly, application of progressively stricter kσ thresholds reveals that the electrical evolution is not characterized by a single onset but by a hierarchical sequence of statistically defined stages. The 2σ exceedance at 12:25 LT represents the earliest objectively defined departure from seasonal background conditions and precedes local particulate enhancement by more than 100 minutes. This phase likely reflects large-scale boundary-layer preconditioning and gradual charge redistribution prior to visible frontal arrival. A 4σ threshold is exceeded at 13:21 LT, marking strengthening beyond moderate variability, while the 5σ exceedance at 13:48 LT coincides with the onset of the rapid-growth regime identified in the high-resolution time series. The ~24-minute separation between the 5σ onset and CST particulate arrival therefore represents a robust operational lead time associated specifically with dynamically forced electrification rather than with low-amplitude baseline fluctuations.

5.2 Bipolar electrical structure of the extreme event

Beyond the lead-time aspect, the event exhibits a well-defined bipolar electrical signature associated with passage of the frontal boundary. PG departs from the seasonal baseline at 12:25 LT and increases progressively to a maximum of +1614 V m^{-1} at 14:10 LT, immediately preceding particulate onset at CST (14:12 LT). Within approximately three minutes, the signal undergoes a rapid inversion to a minimum of −4167 V m^{-1} at 14:13 LT. The resulting peak-to-minimum excursion of ~5.8 kV m^{-1}, together with a maximum one-minute decrease of approximately −2.7 kV m^{-1}, indicates abrupt electric-field reconfiguration rather than gradual conductive relaxation.

The temporal decoupling between the electrical maximum and subsequent $PM_{2.5}$ sub-peaks at CST demonstrates that the strongest electrical perturbation is confined to the frontal interface rather than to the period of maximum surface aerosol mass concentration during the mature phase. This behavior suggests that the bipolar structure reflects organized charge separation at the leading boundary rather than a response governed solely by bulk PM loading. A comparable decoupling between peak aerosol mass and peak electric perturbation was reported during the September 2015 Levant dust outbreak, where multi-day PM enhancement was accompanied by complex and spatially variable electrical behavior rather than a single dominant polarity or amplitude maximum **(Katz et al., 2018).**

Such bipolar surface responses are consistent with organized electrification processes documented in previous field studies. Sequential positive and negative PG disturbances have been observed during advection of inclined dipolar charge structures across fixed sensors in cumulonimbus passages **(Pustovalov & Nagorskiy, 2018).** Vertically resolved measurements during dust storms in northern China identified layered charge structures and multiple polarity reversals **(Zhang et al., 2017)**, and inversion-based reconstructions revealed three-dimensional mosaics of oppositely charged regions coupled to PM_{10} variability **(Zhang & Zhou, 2020).** Although those studies often describe quasi-steady vertical configurations, the present case captures rapid advection of a stratified charge structure across a surface sensor during gust-front passage, producing a transient bipolar ground-level signature rather than a stationary profile.

The amplitude of the excursion (~5.8 kV m^{-1}) lies within the kV m^{-1} range reported for intense dust storms in arid environments. Electrified Sahelian haboobs have exhibited perturbations of 1–10 kV m^{-1} during gust-front passage **(Williams et al., 2008)**, while large-scale Saharan dust intrusions over the eastern Mediterranean have produced Ez fluctuations between +1 and +8 kV m^{-1} (Yair et al., 2016). Tower-based measurements have documented even larger values under specific vertical configurations (Zhang et al., 2017). It should be noted, however, that the corrected minimum value (−4167 V m^{-1}) corresponds to the effective dynamic limit of the measurement system (Section 4.3). The short plateau at this level indicates saturation of the permanent channel (±20 kV m^{-1} full-scale), implying that the true peak negative field during frontal core passage may have exceeded the reported value. This instrumental constraint does not affect timing relationships or polarity structure but indicates that the event intensity is conservatively estimated.

The exceptionally rapid temporal evolution further distinguishes this case. The zero-crossing occurs within a single 5 s sampling interval, and the most intense phase of the inversion unfolds in less than 90 s. Five-second PG data, together with concurrent 10 s meteorological measurements, show that rapid electrical restructuring closely precedes radiative collapse and wind intensification at CST. This ordering indicates that the electrical transition is intrinsically linked to the advancing frontal boundary.

Co-located two-level wind measurements further indicate a transient vertical decoupling during this pre-surge phase. While the lower anemometer (A1, 2 m) recorded near-zero wind immediately prior to the surge, the upper sensor (A2, 10 m) registered sustained non-zero flow. The PG polarity transition occurs within this vertically sheared interval, suggesting that electrical restructuring is embedded in the advancing density-current head prior to the onset of strong near-surface momentum transport.

These observations are consistent with advection of organized space-charge regions within the density current. Vertical charge separation associated with dust lifting and size-dependent particle sorting has been documented in dusty vortices **(Franzese et al., 2018; Esposito et al., 2016)**, where oppositely charged particle populations produce layered electric-field structures. Although the present event involves a density-current dust front rather than an isolated vortex, the observed bipolar PG evolution is consistent with structured charge layering within the advancing frontal system. The absence of additional polarity reversals during later $PM_{2.5}$ sub-peaks reinforces that the most intense electrical gradients were confined to the leading boundary, whereas subsequent particulate enhancements reflect predominantly bulk aerosol transport and sedimentation.

5.3 Physical basis of electrical lead time

The earlier response of PG relative to $PM_{2.5}$ reflects fundamental differences in measurement sensitivity. Particulate sensors quantify mass concentration at the inlet and require sufficient aerosol accumulation to exceed detection thresholds. PG, in contrast, responds to rapid modifications in PG structure driven by charge separation, evolving space-charge distributions, and conductivity contrasts within the advancing density current. Electrical restructuring can therefore precede measurable surface mass enhancement. Field experiments have further demonstrated that atmospheric electric fields generated during saltation can actively enhance dust lifting and exhibit strong feedback with particle emission dynamics **(Esposito et al., 2016)**, reinforcing the physical coupling between electrification and boundary-layer dust processes.

The ~107-minute separation between the initial 2σ deviation at 12:25 LT and CST visual arrival demonstrates that electrical preconditioning begins well before physical intersection of the dust wall. The 5σ rapid-growth onset at 13:48 LT isolates a later, dynamically meaningful phase that precedes particulate arrival by approximately 24 minutes. Together, these statistically constrained stages clarify that electrical lead time is not dependent on a single arbitrary threshold but reflects a physically interpretable hierarchy of boundary-layer evolution.

Convective dust events evolve on minute-scale timescales that are systematically under-resolved by hourly and daily particulate metrics **(Ardon-Dryer, 2025; Ardon-Dryer & Aziz, 2025).** Even sub-hourly monitoring can miss the earliest boundary-layer restructuring associated with frontal development. The present results show that electrical measurements extend detection capability upstream in time relative to particulate concentration thresholds.

PG monitoring has previously been explored as a precursor variable in short-term rainfall nowcasting, with lead times on the order of tens of minutes **(Wu et al., 2023).** Although the charging mechanisms differ between precipitation and dust processes, both involve rapid reorganization of boundary-layer charge structures prior to surface manifestation. The present findings extend this precursor concept to extreme convective dust intrusions.

5.4 Operational implications and limitations

The PG sensor at CST has operated continuously in the hyper-arid desert environment of Ica since 2011, demonstrating long-term robustness under extreme dust loading, thermal variability, and low humidity **(Romero et al., 2024).** While our previous work established the PG response to canonical, wind-driven Paracas events, the 31 July 2025 intrusion serves as an operational stress test under boundary-layer conditions rarely observed in this region. This sustained performance across the entire spectrum of dust dynamics, from ordinary advection to extreme density currents, supports the feasibility of incorporating atmospheric electrical measurements into regional monitoring strategies.

Strategic deployment of PG sensors along dominant upwind corridors could enable tracking of electrical disturbance propagation prior to urban impact. Similar spatial coherence of dust-related electric field disturbances has been documented in multi-station atmospheric electricity networks during Saharan intrusions **(Silva et al., 2016)**, supporting the feasibility of distributed PG monitoring architectures. A distributed configuration spanning initiation zones and receptor sites would complement satellite and particulate systems by providing high-frequency, locally autonomous early indicators not constrained by satellite cadence, dissemination latency, or particulate accumulation thresholds. The approximately 50-minute interval between satellite-constrained frontal formation south of the corridor and surface impact at CST further illustrates the potential expansion of actionable lead time within a distributed monitoring framework.

Several limitations must nevertheless be acknowledged. Because haboob-like intrusions are historically rare in the study area, the present analysis is restricted to a single extreme event and does not establish climatological generality for this specific frontal geometry. Electrical responses may vary with humidity, stability, background aerosol loading, and dust mineralogy. Vertical charge distributions were not directly measured during this event; the bipolar interpretation is therefore inferred from surface PG evolution and supported by analogous observations in other dust regimes **(Mallios et al., 2023).** Satellite RGB imagery provides qualitative spatial context but limited quantitative concentration information.

To assess short-term operational robustness under seasonally consistent conditions, the same kσ + 5-min persistence framework was applied to the 30 days preceding 31 July 2025 within the identical 12:00–14:15 LT window. A single non-event day exhibited a 5σ crossing; however, that crossing was not followed by sustained PG amplification and remained confined to background-scale variability. In contrast, the 31 July event was characterized by rapid and persistent post-threshold growth culminating in the largest excursion of the multi-year record.

This contrast highlights an important operational distinction: high-sigma crossings alone do not define extreme events; rather, the dynamical evolution following threshold exceedance determines physical significance. Within this framework, the 5σ level functions as a transition marker into rapid electrical growth rather than as a purely binary alarm. Although the 30-day window does not establish climatological skill, it demonstrates that sustained post-onset amplification is not a routine feature of July background variability.

Despite these limitations, the convergence of satellite tracking, camera-based arrival times, particulate onset, and high-resolution electrical evolution defines a robust temporal hierarchy. The event demonstrates that electrical restructuring begins well before visual frontal arrival, that the strongest electric perturbation is associated with the leading boundary rather than peak mass loading, and that extreme dust fronts can exhibit bipolar electrical signatures distinct from common Paracas events. Although the exceptionally rare nature of this event precludes robust long-term statistical validation of false alarm rates for haboob detections, this measurable timing advantage is consistent with high PG sensitivity under rapid-evolution conditions. This motivates the integration of PG monitoring as a complementary component of operational dust nowcasting systems in arid regions, capable of bridging the temporal gap between satellite imagery and surface PM accumulation.

6. Conclusions

The 31 July 2025 dust event demonstrates that PG measurements can detect rapidly evolving dust intrusions substantially earlier than conventional mass-based particulate sensors. Using a seasonal baseline framework, electrical restructuring at CST preceded local $PM_{2.5}$ enhancement by approximately 24 minutes under a conservative 5σ rapid-growth criterion and by more than 100 minutes relative to the initial 2σ departure. Independent constraints from satellite tracking, inter-station propagation, and camera-defined arrival confirm a coherent southwest-to-northeast progression and validate the temporal robustness of the detection sequence.

Beyond lead time, the event exhibited a pronounced bipolar electrical structure, characterized by progressive PG amplification prior to frontal impact followed by an abrupt polarity reversal coincident with particulate onset. Relative to the 2018–2025 multi-year record, this case produced the largest daily electrical excursion in the available climatology, exceeding the 99.9th percentile of both maximum absolute PG and peak-to-trough variability. Multi-resolution measurements confirm that the polarity transition represents a rapidly evolving physical restructuring rather than an artifact of temporal averaging.

Satellite imagery provided essential regional context but was constrained by acquisition cadence and dissemination latency. In contrast, continuous high-resolution PG monitoring captured early boundary-layer electrical restructuring independent of external data pipelines. This capability highlights the potential operational value of atmospheric electricity measurements during extreme dust-front events.

These findings indicate that atmospheric electrical measurements can extend actionable lead time during extreme dust-front events while providing physically distinct information on frontal electrical structure. Strategically deployed PG sensors along dominant upwind corridors, for example within a simple multi-station geometry, could enhance early-warning capability and constrain front progression in real time, complementing existing satellite and particulate monitoring systems. Rather than a statistical limitation, the exceptionally rare nature of this historic haboob provides a stringent stress test for the baseline established in the region. The internally consistent multi-platform timing relationships support a clear detection advantage of PG in this event. This case indicates that continuous PG monitoring can bridge the temporal gap during extreme boundary-layer anomalies, providing crucial early warnings where conventional mass-based systems and satellites experience critical latency.

Given the recurrent dust activity along the southern Peruvian coastal corridor, the absence of dedicated atmospheric electrical monitoring represents a missed opportunity for early detection of rapidly evolving density-current dust fronts.

Appendix A. Satellite-based kinematic analysis of dust-front propagation

To quantify regional dust-front translation, leading-edge positions were manually tracked at 10-minute intervals from GOES-19 RGB imagery along the trajectories directed toward the STG and CST sectors. For each pair of consecutive frames, the great-circle displacement between front-edge coordinates was computed using the haversine formulation. Interval propagation speed was then obtained as the ratio between displacement and elapsed time. For clarity, each 10-minute interval speed is reported at the end time of the corresponding interval (e.g., the 13:20–13:30 LT speed is plotted at 13:30 LT). The resulting frame-to-frame translation rates are shown in **Figure A1**, where panel (a) corresponds to the STG-directed trajectory and panel (b) to the CST-directed trajectory. Because satellite sampling is discrete, the derived velocities represent interval-averaged frontal translation rather than instantaneous speeds.

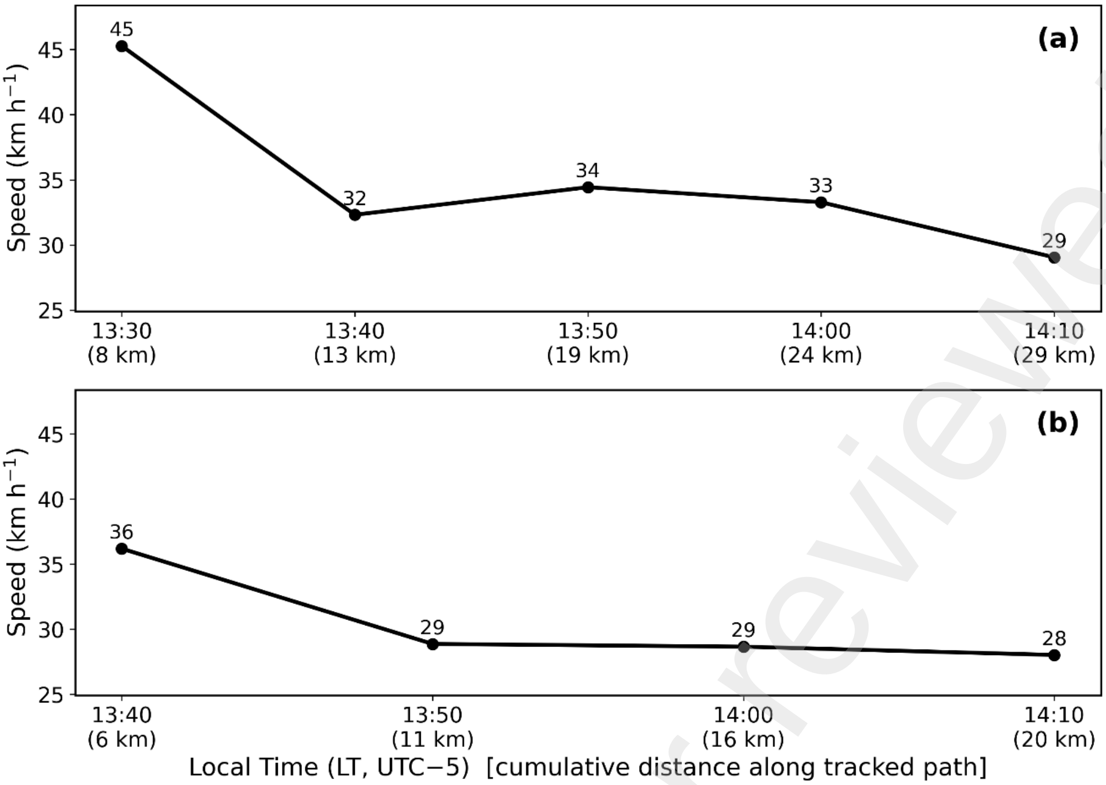

Figure A1. Frame-to-frame propagation speeds of the tracked dust-front leading edge derived from consecutive GOES-19 RGB images (10-minute cadence). Panel (a) shows the STG-directed trajectory; panel (b) shows the CST-directed trajectory.

The 13:20–13:30 LT interval along the STG-directed trajectory yields a displacement of 7.6 km over 10 minutes, corresponding to 12.67 m s^{-1} (45.6 km h^{-1}), consistent with the regional propagation velocity reported in Section 4.1. This value is plotted at 13:30 LT, reflecting the end of the first measurable interval following the initial identification of the dust front at 13:20 LT. The CST-directed segment becomes clearly identifiable beginning in the 13:30 LT frame, indicating that the plume impacting CST organized approximately 10 minutes after the initial STG-directed segment was established. Consequently, the first CST velocity estimate corresponds to the 13:30–13:40 LT interval and is plotted at 13:40 LT in **Figure A1**. Subsequent intervals exhibit comparable magnitudes along both trajectories, supporting a coherent mesoscale southwest-to-northeast propagation of the evolving dust-front system rather than strict translation of a single rigid boundary. The similarity between the STG- and CST-directed interval speeds indicates dynamically organized frontal evolution across the monitoring corridor.

Uncertainty is primarily controlled by the 10-minute temporal resolution of the imagery and by manual identification of the leading edge within each frame. These factors constrain temporal precision but do not materially affect the order-of-magnitude estimate of frontal translation speed.

Appendix B. High-resolution electrical and surface meteorological timing

To document the sub-minute sequencing of electrical and surface meteorological signals during the 31 July 2025 intrusion, 5 s PG measurements were analyzed together with 10 s solar irradiance and co-located wind observations from two anemometers mounted on the same tower within the 14:08–14:15 LT interval. Wind data are shown for anemometer A1 (2 m height) and anemometer A2 (10 m height), providing wind speed and wind direction measurements. Figure B1 presents the synchronized time series used to determine the timing values reported in Section 4.3. Vertical dashed lines indicate (i) the PG maximum time, (ii) the PG polarity-reversal time, and (iii) the onset of the irradiance decrease and near-surface wind intensification.

The two-level wind record shows that A1 records a short low-wind interval immediately prior to the main wind surge, whereas A2 maintains sustained non-zero flow over the same period. Wind direction at both levels exhibits substantial variability prior to 14:11 LT and subsequently becomes more consistently aligned during the wind-intensification phase after 14:12 LT. This appendix documents the high-resolution timing framework supporting the analysis presented in Section 4.3.

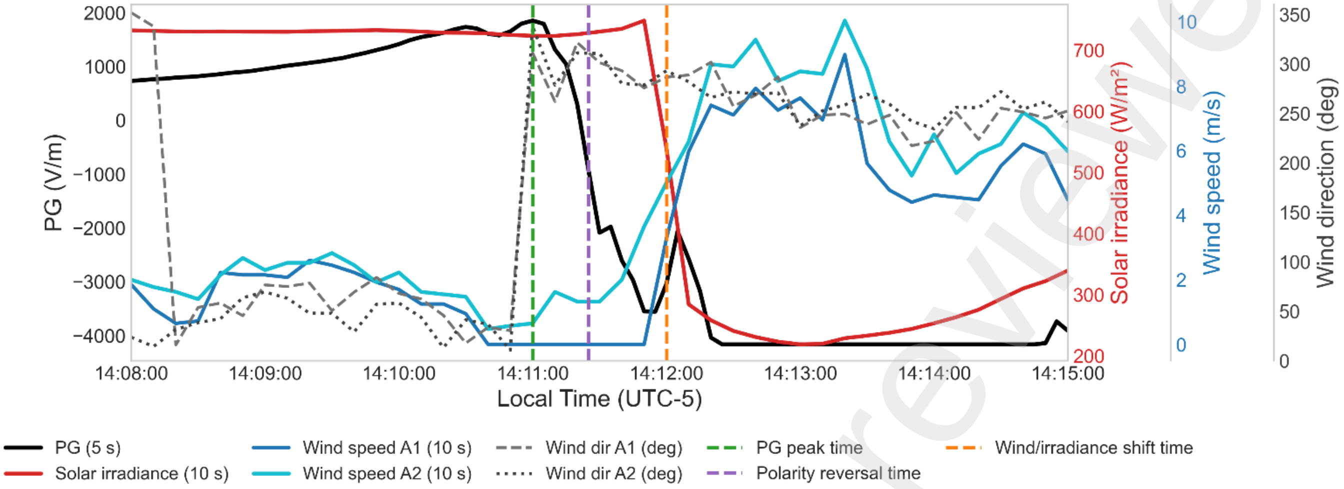

Figure B1. High-resolution PG (5 s), solar irradiance (10 s), wind speed (10 s), and wind direction (10 s) during 14:08–14:15 LT on 31 July 2025. Wind observations are shown at two heights on the same tower: A1 (2 m) and A2 (10 m). Vertical dashed lines indicate the PG maximum, the polarity reversal, and the onset of the irradiance decrease and near-surface wind intensification.

Appendix C. Electrical regime comparison between canonical Paracas events and the 31 July 2025 extreme dust intrusion

To compare the electrical structure of the 31 July 2025 event with typical Paracas dust episodes, a PG-only epoch analysis was performed using 12 canonical Paracas events selected from the dataset analyzed in Romero et al. (2024). These events occurred on 23 July 2019, 3 October 2019, 5 October 2019, 26 November 2019, 1 December 2019, 10 January 2020, 1 September 2020, 23 October 2021, 7 December 2021, 10 January 2022, 12 January 2022, and 13 January 2022. Because particulate data are only available for 31 July 2025, the comparison is restricted to PG measurements.

For each canonical event, the PG minimum within the documented event window was identified, and a ±60 min interval centered on the time of minimum PG (t_{min}) was extracted. The same procedure was applied to the 31 July 2025 event. **Figure C1** shows the superposed epoch curves. Canonical Paracas events exhibit predominantly monopolar negative excursions centered on t_{min}. In contrast, the 31 July 2025 event displays a structured bipolar evolution characterized by a pre-minimum positive enhancement followed by a rapid polarity reversal. This electrical-only comparison indicates that the 31 July 2025 intrusion differs structurally from the canonical Paracas regime described in Romero et al. (2024).

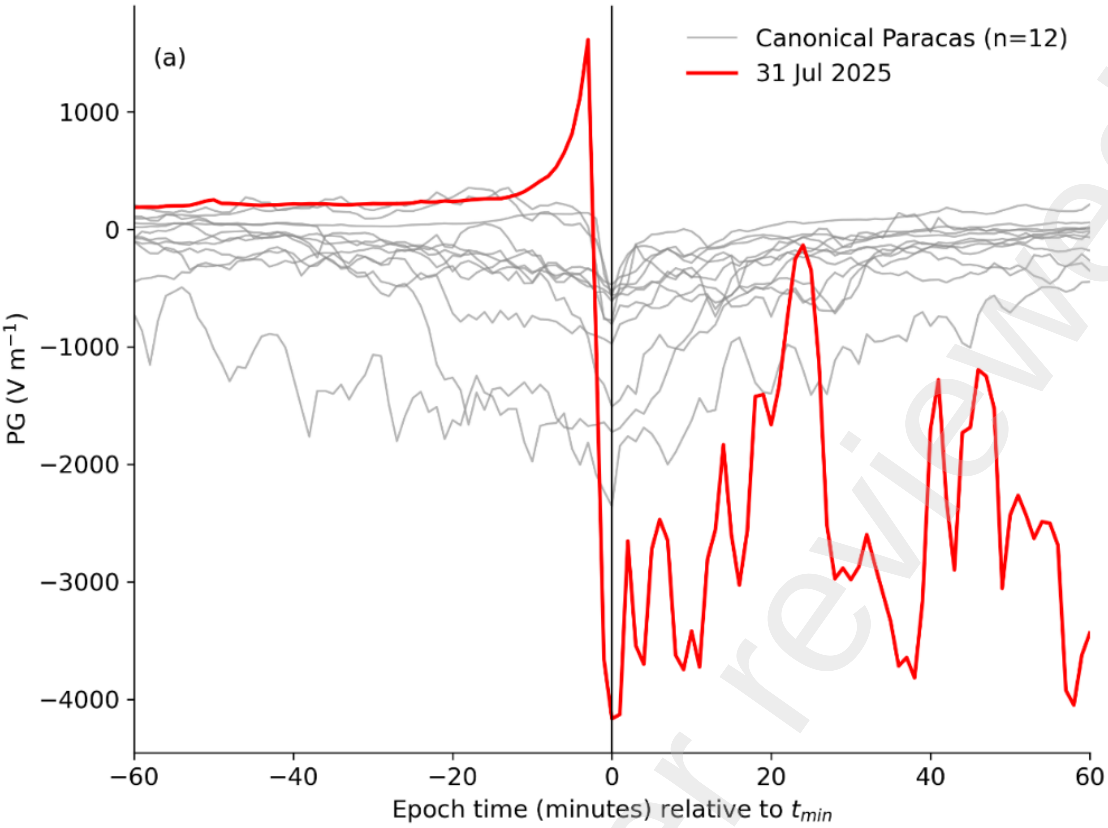

Figure C1. Epoch alignment of PG centered on the time of the daily PG minimum (t_{min}) for canonical Paracas events (gray) and the 31 July 2025 intrusion (red). Curves represent ±60 min relative to t_{min}. Canonical events show predominantly monopolar negative excursions, whereas the 31 July 2025 case exhibits a structured bipolar evolution with pre-minimum positive enhancement and rapid polarity reversal.

Acknowledgements

RR expresses gratitude to CNPq (Proc. 141576/2023-5 - GD). JPR thanks funding agencies CNPq (project:311927/2022-0) and CAPES (project:88881.310386/2018-697 01). J.T. acknowledges funding from the National Science Centre, Poland (Grant No. 2023/51/D/ST10/01757).

RR, RL, GO, YB, and JA acknowledge institutional support from the Universidad Nacional San Luis Gonzaga (UNICA) and the Centro de Investigación de la Actividad Solar y sus Efectos sobre la Tierra (CIEASEST). The monitoring infrastructure and instrumentation supporting this study were established through a competitive research grant awarded in 2023 by the Vicerrectorado de Investigación (VRI), UNICA. The near-real-time monitoring platform associated with this infrastructure is maintained by the authors.

Declaration of competing interests

The authors declare that they have no competing interests.

Data availability statement

PG data belonging to the Atmospheric Electric Field Network in South America (AFINSA), together with the ground-based camera sequences used to determine visual dust-front arrival times, are archived in a Zenodo repository (https://doi.org/10.5281/zenodo.18881269).

PM and meteorological data are available from the Research Center for the Study of Solar Activity and its Effects on Earth (CIEASEST), Universidad Nacional San Luis Gonzaga (UNICA): https://cieasest.unica.edu.pe/

Satellite data from the NOAA Geostationary Operational Environmental Satellites (GOES-19) were accessed via the NOAA Open Data Registry: https://registry.opendata.aws/noaa-goes/

A near-real-time visualization platform associated with the monitoring stations is maintained at https://www.aireica.com/.

Code availability

The code used in this study is available from the corresponding author upon reasonable request.

References

Ardon-Dryer, K., 2025. Minute-scale convective dust events are overlooked in urban air quality monitoring. Commun Earth Environ 6, 815. https://doi.org/10.1038/s43247-025-02836-7

Ardon-Dryer, K., Aziz, T., 2025. Times Matter, the Impact of Convective Dust Events on Air Quality in the Greater Phoenix Area, Arizona. GeoHealth 9, e2024GH001209. https://doi.org/10.1029/2024GH001209

Bouet, C., Labiadh, M.T., Rajot, J.L., Bergametti, G., Marticorena, B., Henry Des Tureaux, T., Ltifi, M., Sekrafi, S., Féron, A., 2019. Impact of Desert Dust on Air Quality: What is the Meaningfulness of Daily PM Standards in Regions Close to the Sources? The Example of Southern Tunisia. Atmosphere 10, 452. https://doi.org/10.3390/atmos10080452

Briceño-Zuluaga, F., Castagna, A., Rutllant, J.A., Flores-Aqueveque, V., Caquineau, S., Sifeddine, A., Velazco, F., Gutierrez, D., Cardich, J., 2017. Paracas dust storms: Sources, trajectories and associated meteorological conditions. Atmospheric Environment 165, 99–110. https://doi.org/10.1016/j.atmosenv.2017.06.019

Chalmers, J.A., 1954. Atmospheric Electricity. Rep. Prog. Phys. 17, 101–134. https://doi.org/10.1088/0034-4885/17/1/303

El Comercio, 2025. Gigantesca tormenta de arena cubre Ica, Nasca, Pisco y Paracas. 31 July 2025. https://elcomercio.pe/peru/ica/ica-reportan-tormenta-de-arena-que-cubre-tambien-pisco-paracas-y-nasca-ultimas-noticia/ (accessed 24 February 2026).

Esposito, F., Molinaro, R., Popa, C.I., Molfese, C., Cozzolino, F., Marty, L., Taj-Eddine, K., Di Achille, G., Franzese, G., Silvestro, S., Ori, G.G., 2016. The role of the atmospheric electric field in the dust-lifting process. Geophysical Research Letters 43, 5501–5508. https://doi.org/10.1002/2016GL068463

Franzese, G., Esposito, F., Lorenz, R., Silvestro, S., Popa, C.I., Molinaro, R., Cozzolino, F., Molfese, C., Marty, L., Deniskina, N., 2018. Electric properties of dust devils. Earth and Planetary Science Letters 493, 71–81. https://doi.org/10.1016/j.epsl.2018.04.023

Gay, S.P., 2005. Blowing sand and surface winds in the Pisco to Chala Area, Southern Peru. Journal of Arid Environments 61, 101–117. https://doi.org/10.1016/j.jaridenv.2004.07.012

Harris, D.J., 1967. Electrical Effects of the Harmattan Dust Storms. Nature 214, 585–585. https://doi.org/10.1038/214585a0

Harrison, R.G., 2013. The Carnegie Curve. Surv Geophys 34, 209–232. https://doi.org/10.1007/s10712-012-9210-2

Kamra, A.K., 1972. Measurements of the electrical properties of dust storms. J. Geophys. Res. 77, 5856–5869. https://doi.org/10.1029/JC077i030p05856

Katz, S., Yair, Y., Price, C., Yaniv, R., Silber, I., Lynn, B., Ziv, B., 2018. Electrical properties of the 8–12th September, 2015 massive dust outbreak over the Levant. Atmospheric Research 201, 218–225. https://doi.org/10.1016/j.atmosres.2017.11.004

Mallios, S., Daskalopoulou, V., Spanakis-Misirlis, V., Hloupis, G., Amiridis, V., 2023. Novel Measurements of Desert Dust Electrical Properties: A Multi-Instrument Approach during the ASKOS 2022 Campaign, in: COMECAP 2023. Presented at the COMECAP 2023, MDPI, p. 22. https://doi.org/10.3390/environsciproc2023026022

NASA Earth Observatory, 2025. *Dust engulfs coastal Peru*. Image of the Day, 5 August 2025. https://science.nasa.gov/earth/earth-observatory/dust-engulfs-coastal-peru-154637/ (accessed 24 February 2026).

Nicoll, K.A., Harrison, R.G., Silva, H.G., Salgado, R., Melgâo, M., Bortoli, D., 2018. Electrical sensing of the dynamical structure of the planetary boundary layer. Atmospheric Research 202, 81–95. https://doi.org/10.1016/j.atmosres.2017.11.009

Pustovalov, K.N., Nagorskiy, P.M., 2018. Response in the surface atmospheric electric field to the passage of isolated air mass cumulonimbus clouds. Journal of Atmospheric and Solar-Terrestrial Physics 172, 33–39. https://doi.org/10.1016/j.jastp.2018.03.008

Raman, A., Arellano, A.F., Brost, J.J., 2014. Revisiting haboobs in the southwestern United States: An observational case study of the 5 July 2011 Phoenix dust storm. Atmospheric Environment 89, 179–188. https://doi.org/10.1016/j.atmosenv.2014.02.026

Romero, R., Tacza, J., Arroyo, J., Prieto, F., Macotela, L., Buleje, Y., Loayza, R., Fernandez, U., Raulin, J.-P., 2024. First results of the potential gradient variation in a tropical station in South America (Ica, Peru). Journal of Atmospheric and Solar-Terrestrial Physics 256, 106198. https://doi.org/10.1016/j.jastp.2024.106198

Romero Ramirez, R.M. (2026) «Atmospheric Potential Gradient Measurements (5-second resolution) and Camera Observations During the 31 July 2025 Dust-Front Event in Ica, Peru». Zenodo. doi:10.5281/zenodo.18881269.

Rycroft, M.J., Israelsson, S., Price, C., 2000. The global atmospheric electric circuit, solar activity and climate change. Journal of Atmospheric and Solar-Terrestrial Physics 62, 1563–1576. https://doi.org/10.1016/S1364-6826(00)00112-7

Schmit, T.J., Gunshor, M.M., Menzel, W.P., Gurka, J.J., Li, J., Bachmeier, A.S., 2005. INTRODUCING THE NEXT-GENERATION ADVANCED BASELINE IMAGER ON GOES-R. Bull. Amer. Meteor. Soc. 86, 1079–1096. https://doi.org/10.1175/BAMS-86-8-1079

Silva, H.G., Lopes, F.M., Pereira, S., Nicoll, K., Barbosa, S.M., Conceição, R., Neves, S., Harrison, R.G., Collares Pereira, M., 2016. Saharan dust electrification perceived by a triangle of atmospheric electricity stations in Southern Portugal. Journal of Electrostatics 84, 106–120. https://doi.org/10.1016/j.elstat.2016.10.002

Stow, C.D., 1969. Dust And Sand Storm Electrification. Weather 24, 134–144. https://doi.org/10.1002/j.1477-8696.1969.tb03165.x

Tacza, J., Raulin, J.-P., Macotela, E., Norabuena, E., Fernandez, G., Correia, E., Rycroft, M.J., Harrison, R.G., 2014. A new South American network to study the atmospheric electric field and its variations related to geophysical phenomena. Journal of Atmospheric and Solar-Terrestrial Physics 120, 70–79. https://doi.org/10.1016/j.jastp.2014.09.001

Tacza, J.C., 2015. *Análise do campo elétrico atmosférico durante tempo bom e distúrbios geofísicos*. Master’s dissertation. Universidade Presbiteriana Mackenzie, São Paulo. Available at: http://dspace.mackenzie.br/handle/10899/24124.

Williams, E., Nathou, N., Hicks, E., Pontikis, C., Russell, B., Miller, M., Bartholomew, M.J., 2009. The electrification of dust-lofting gust fronts (‘haboobs’) in the Sahel. Atmospheric Research 91, 292–298. https://doi.org/10.1016/j.atmosres.2008.05.017

Wilson, C.T.R., 1921. III. Investigations on lighting discharges and on the electric field of thunderstorms. Philosophical Transactions of the Royal Society of London. Series A, Containing Papers of a Mathematical or Physical Character 221, 73–115. https://doi.org/10.1098/rsta.1921.0003

Wu, J., Zou, Z., Li, Y., Xie, F., 2024. The possibility of rainfall nowcasting using atmospheric electric field. Atmospheric Research 298, 107118. https://doi.org/10.1016/j.atmosres.2023.107118

Yair, Y., Katz, S., Yaniv, R., Ziv, B., Price, C., 2016. An electrified dust storm over the Negev desert, Israel. Atmospheric Research 181, 63–71. https://doi.org/10.1016/j.atmosres.2016.06.011

Zhang, H., Bo, T.-L., Zheng, X., 2017. Evaluation of the electrical properties of dust storms by multi-parameter observations and theoretical calculations. Earth and Planetary Science Letters 461, 141–150. https://doi.org/10.1016/j.epsl.2017.01.001

Zhang, H., Zhou, Y.-H., 2020. Reconstructing the electrical structure of dust storms from locally observed electric field data. Nat Commun 11, 5072. https://doi.org/10.1038/s41467-020-18759-0

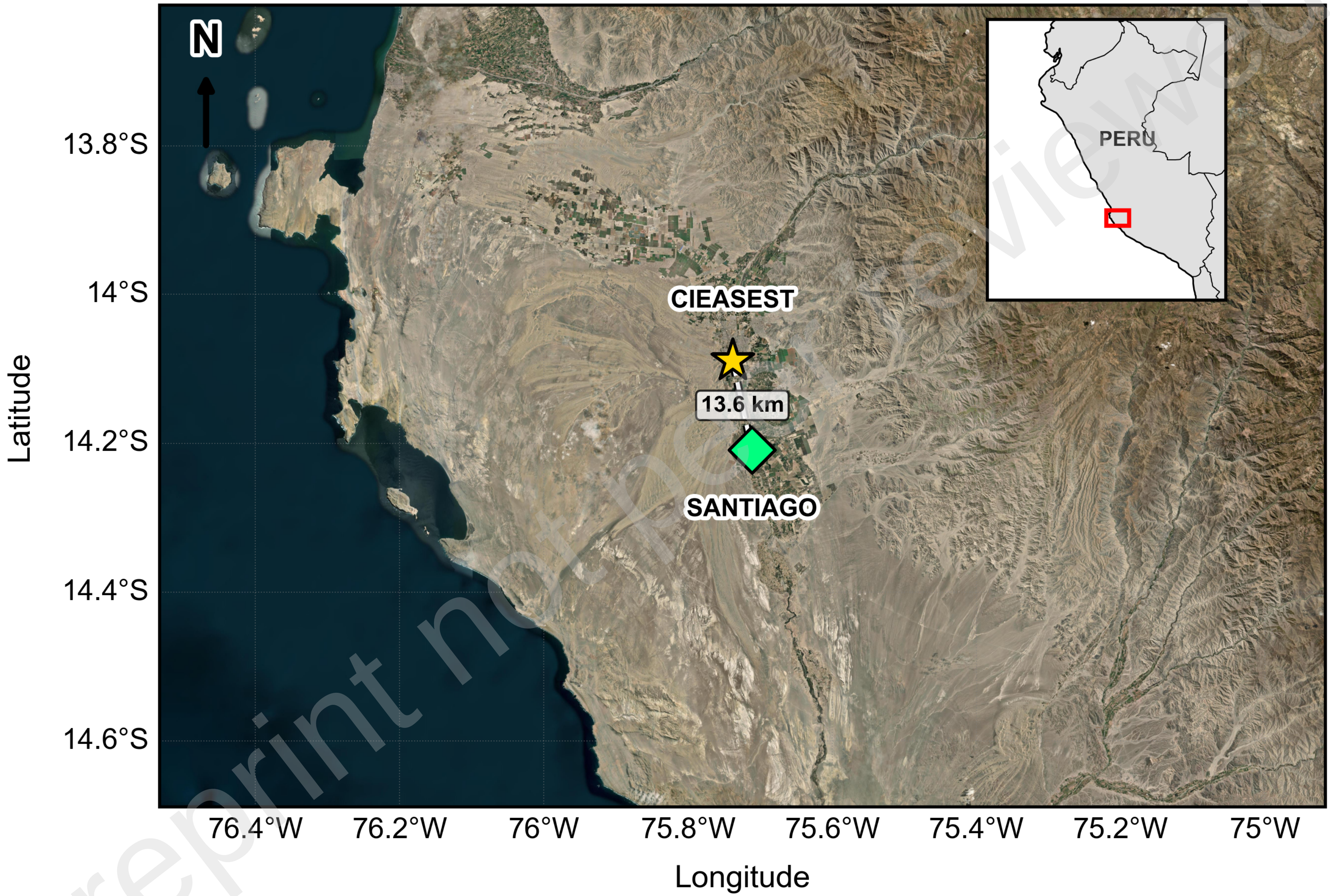
N
PERU
CIEASEST
13.6 km
SANTIAGO
13.8°S
14°S
14.2°S
14.4°S
14.6°S
Latitude
76.4°W
76.2°W
76°W
75.8°W
75.6°W
75.4°W
75.2°W
75°W
Longitude

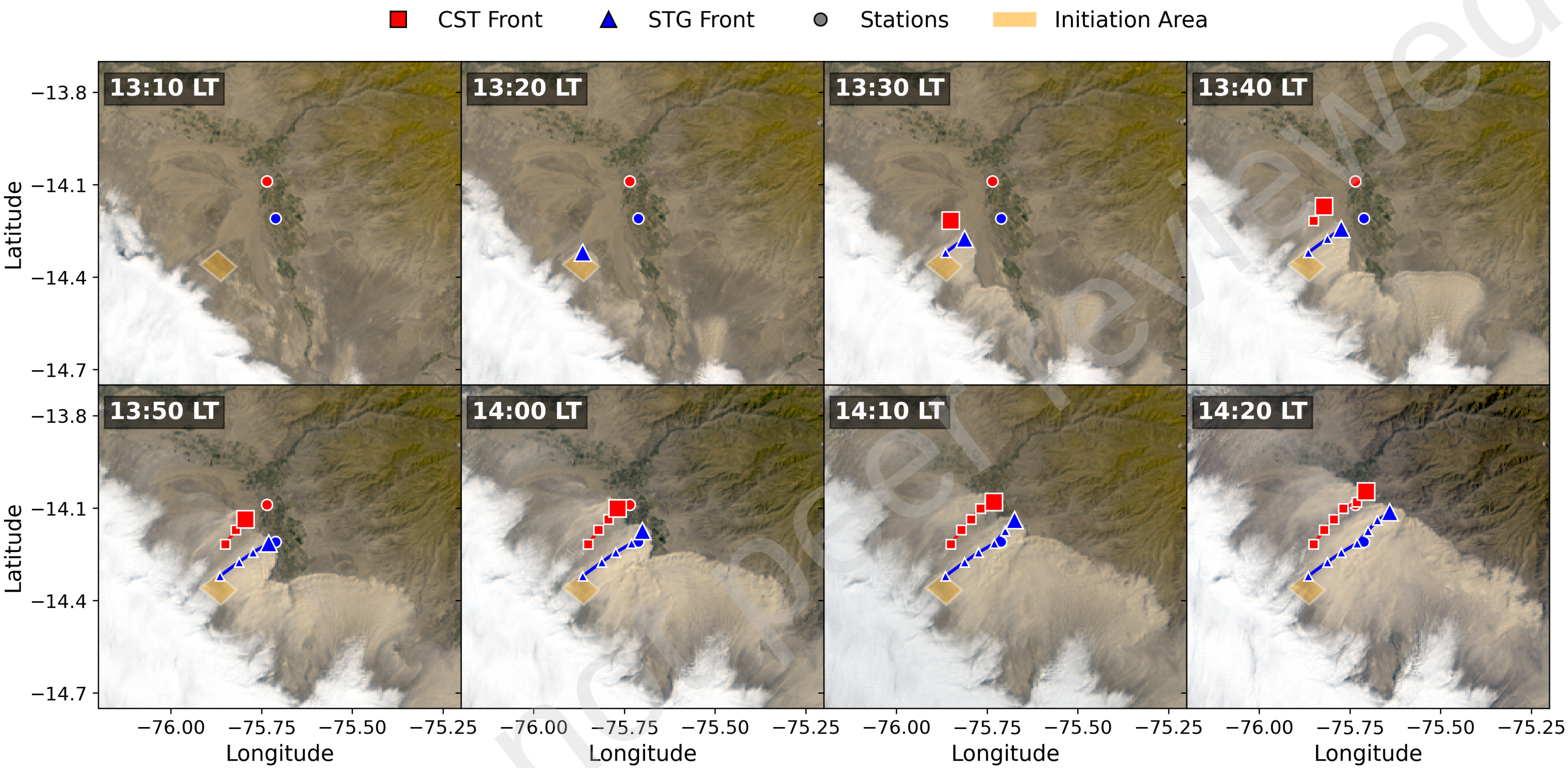
CST Front
STG Front
Stations
Initiation Area
13:10 LT
13:20 LT
13:30 LT
13:40 LT
13:50 LT
14:00 LT
14:10 LT
14:20 LT
−13.8
−14.1
−14.4
−14.7
Latitude
−76.00
−75.75
−75.50
−75.25
Longitude

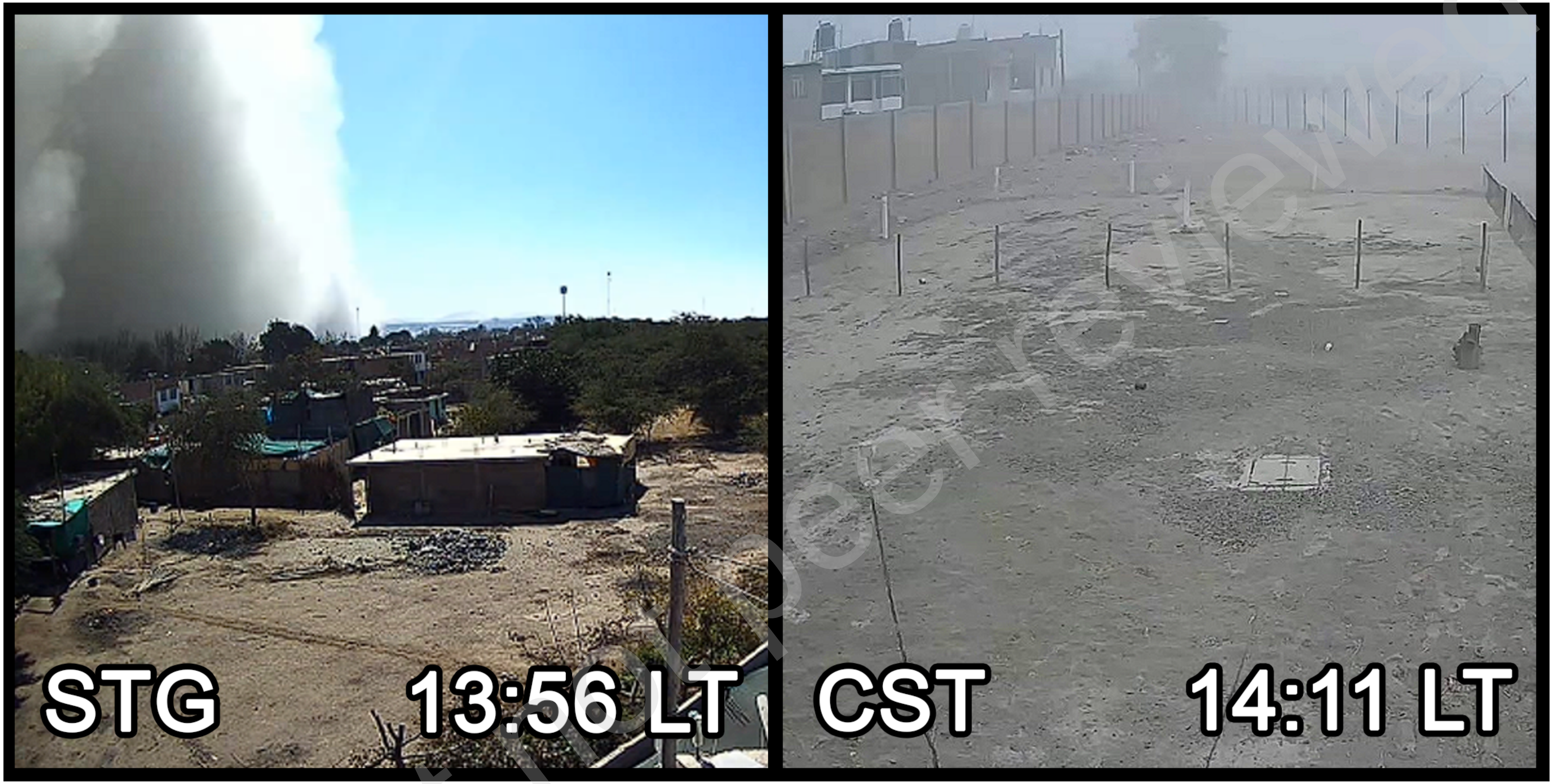
STG
13:56 LT
CST
14:11 LT

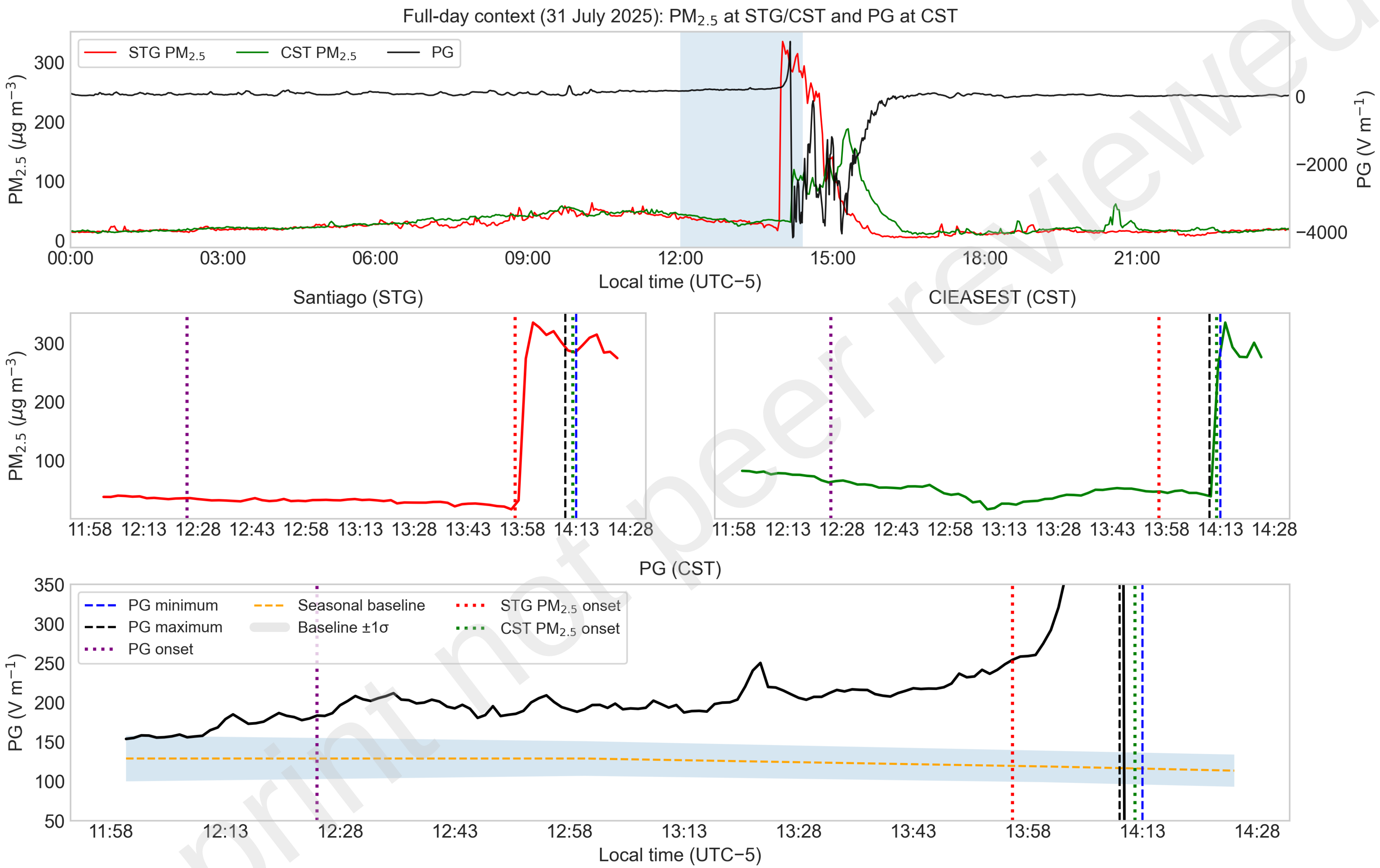
Full-day context (31 July 2025): $PM_{2.5}$ at STG/CST and PG at CST
STG $PM_{2.5}$
CST $PM_{2.5}$
PG
$PM_{2.5}$ ($\mu g\ m^{-3}$)
PG ($V\ m^{-1}$)
0
100
200
300
0
−2000
−4000
00:00
03:00
06:00
09:00
12:00
15:00
18:00
21:00
Local time (UTC−5)
Santiago (STG)
CIEASEST (CST)
$PM_{2.5}$ ($\mu g\ m^{-3}$)
100
200
300
11:58
12:13
12:28
12:43
12:58
13:13
13:28
13:43
13:58
14:13
14:28
PG (CST)
PG minimum
PG maximum
PG onset
Seasonal baseline
Baseline ±1σ
STG $PM_{2.5}$ onset
CST $PM_{2.5}$ onset
PG ($V\ m^{-1}$)
50
100
150
200
250
300
350
11:58
12:13
12:28
12:43
12:58
13:13
13:28
13:43
13:58
14:13
14:28
Local time (UTC−5)

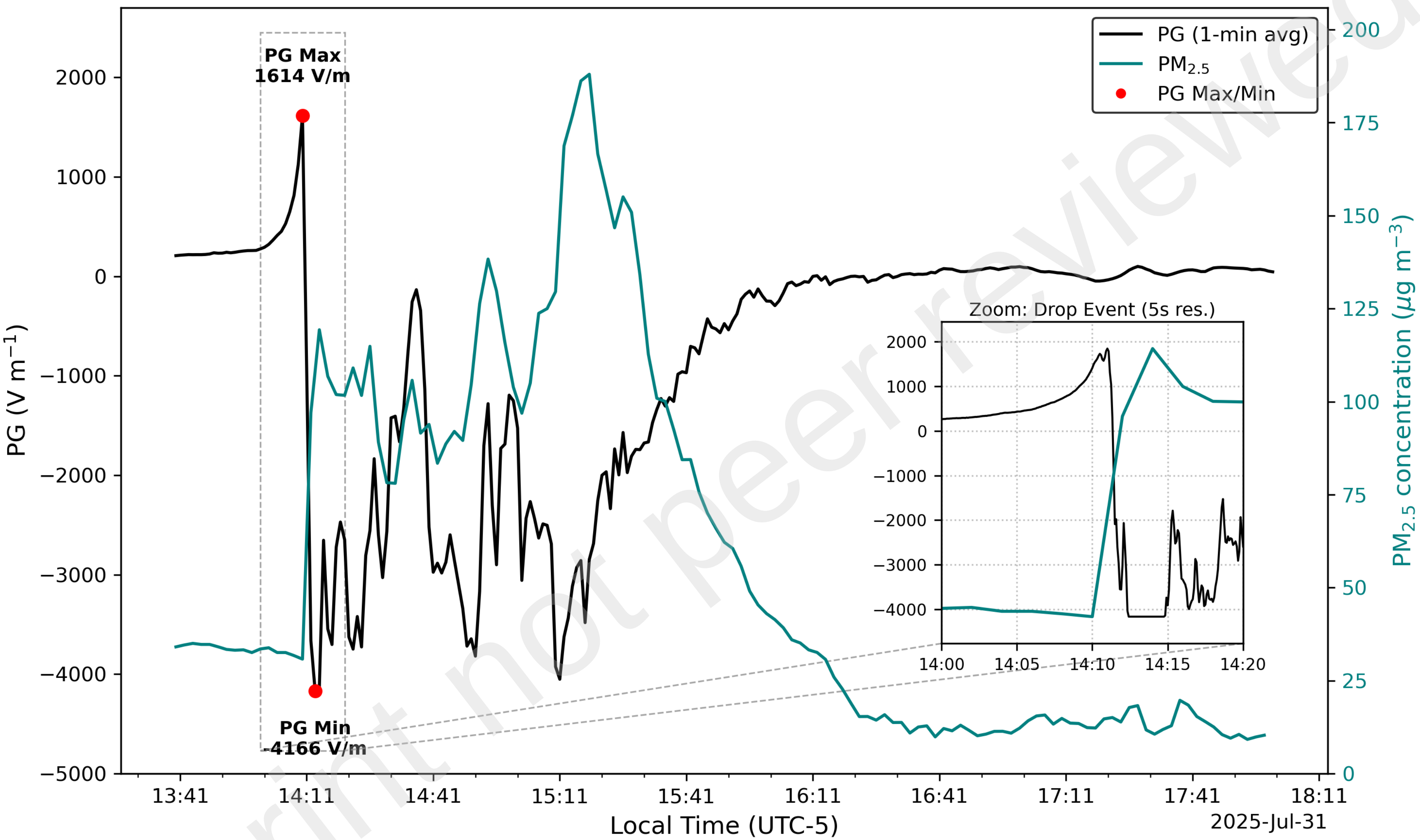
PG Max
1614 V/m
PG Min
-4166 V/m
PG (1-min avg)
$PM_{2.5}$
PG Max/Min
Zoom: Drop Event (5s res.)
2000
1000
0
−1000
−2000
−3000
−4000
14:00
14:05
14:10
14:15
14:20
PG (V m^{-1})
2000
1000
0
−1000
−2000
−3000
−4000
−5000
13:41
14:11
14:41
15:11
15:41
16:11
16:41
17:11
17:41
18:11
Local Time (UTC-5)
2025-Jul-31
$PM_{2.5}$ concentration ($\mu g\ m^{-3}$)
200
175
150
125
100
75
50
25
0

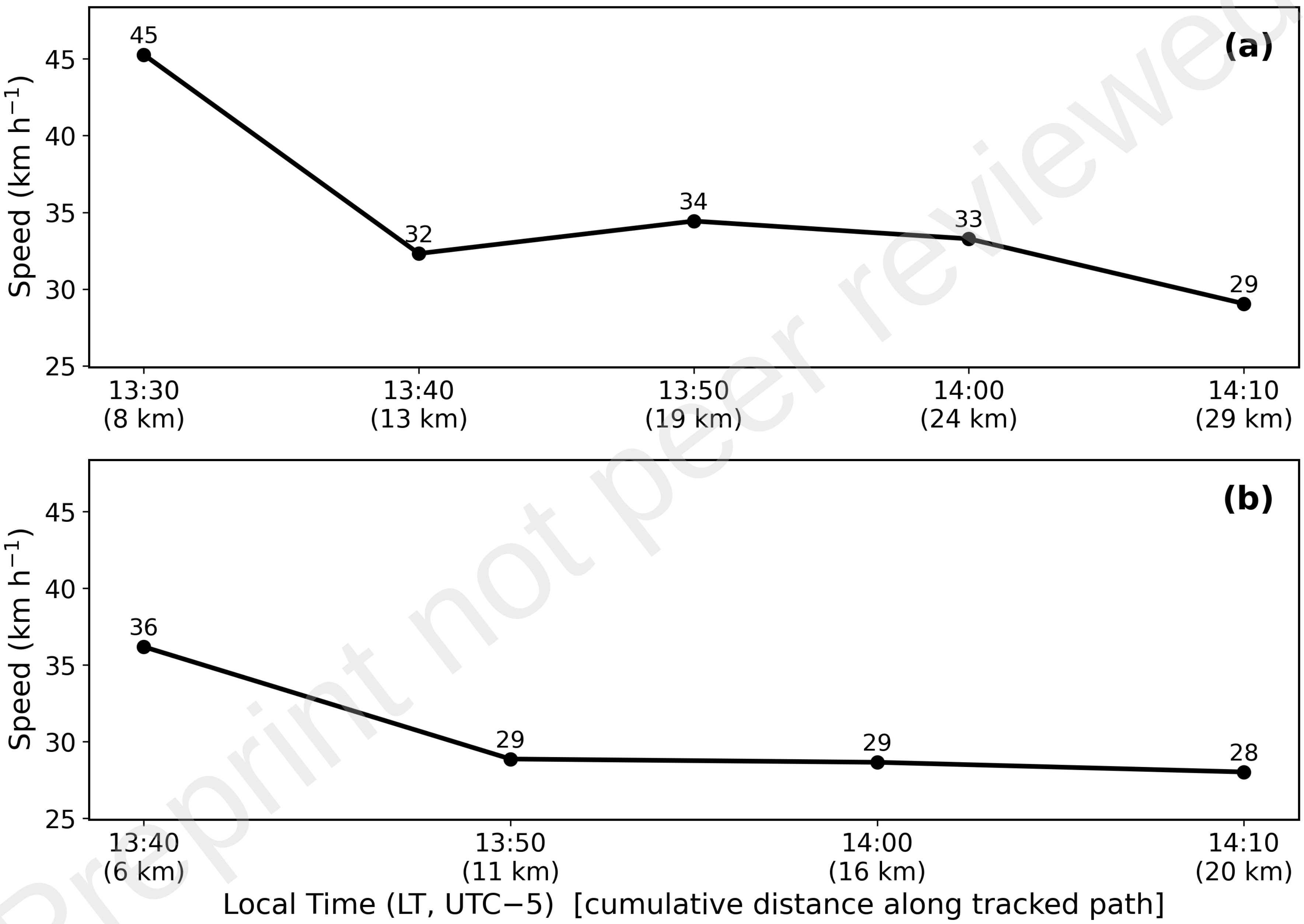
(a)
Speed (km h^{-1})
45
40
35
30
25
45
32
34
33
29
13:30 (8 km)
13:40 (13 km)
13:50 (19 km)
14:00 (24 km)
14:10 (29 km)
(b)
Speed (km h^{-1})
45
40
35
30
25
36
29
29
28
13:40 (6 km)
13:50 (11 km)
14:00 (16 km)
14:10 (20 km)
Local Time (LT, UTC−5) [cumulative distance along tracked path]

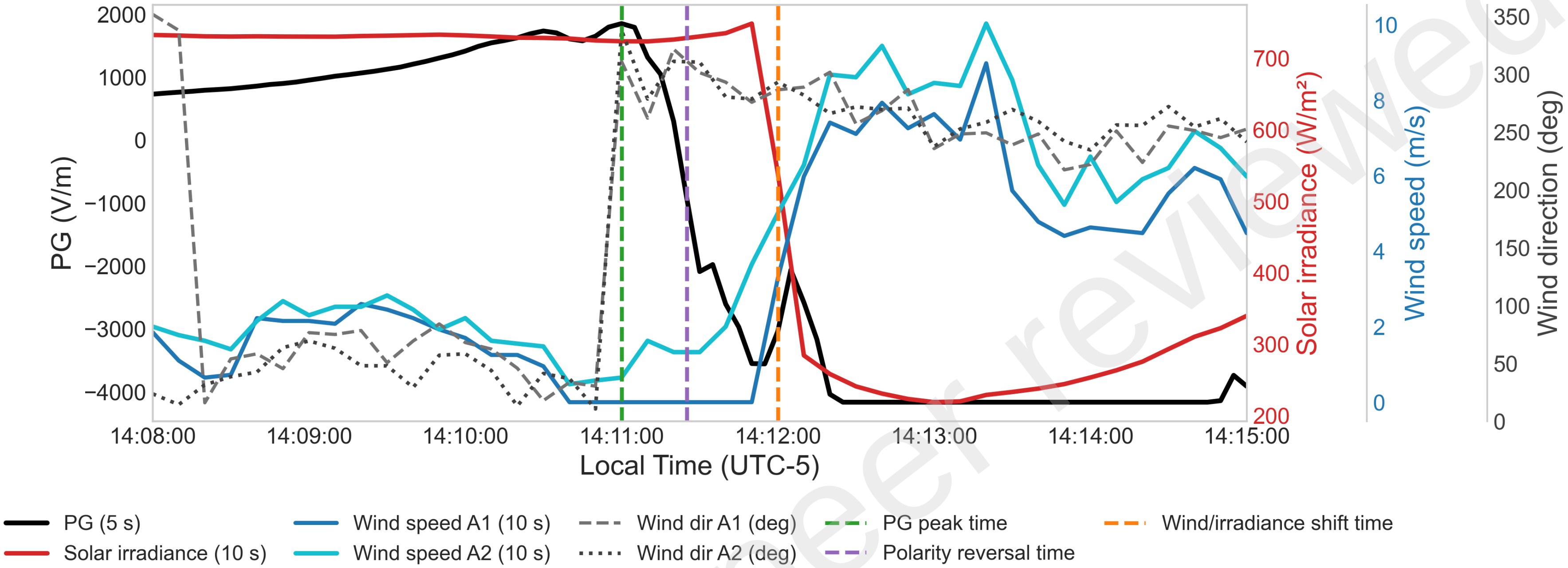
PG (V/m)
2000
1000
0
−1000
−2000
−3000
−4000
Solar irradiance (W/m²)
700
600
500
400
300
200
Wind speed (m/s)
10
8
6
4
2
0
Wind direction (deg)
350
300
250
200
150
100
50
0
14:08:00
14:09:00
14:10:00
14:11:00
14:12:00
14:13:00
14:14:00
14:15:00
Local Time (UTC-5)
PG (5 s)
Solar irradiance (10 s)
Wind speed A1 (10 s)
Wind speed A2 (10 s)
Wind dir A1 (deg)
Wind dir A2 (deg)
PG peak time
Polarity reversal time
Wind/irradiance shift time

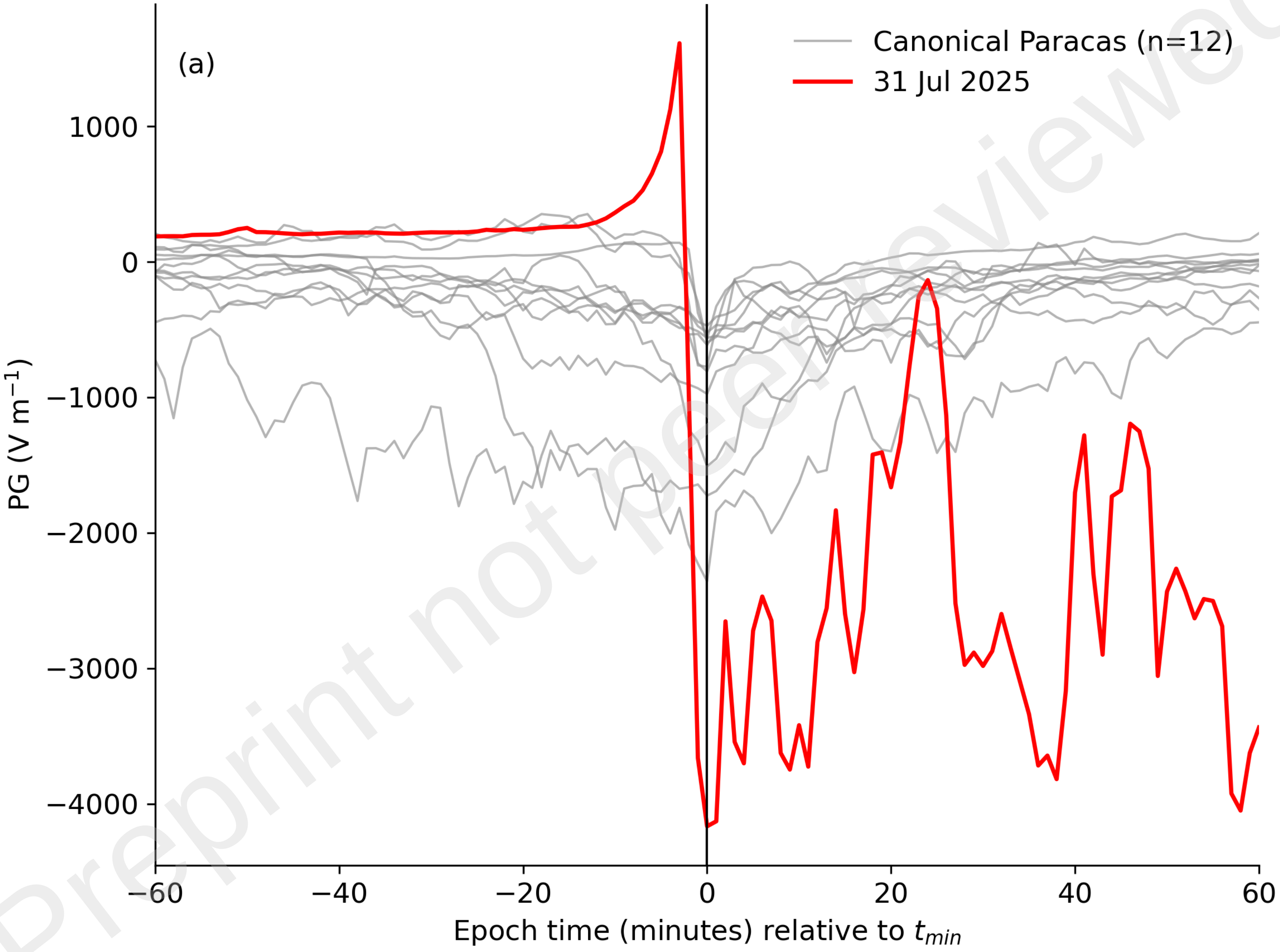
(a)
Canonical Paracas (n=12)
31 Jul 2025
1000
0
−1000
−2000
−3000
−4000
PG (V m^{-1})
−60
−40
−20
0
20
40
60
Epoch time (minutes) relative to t_{min}